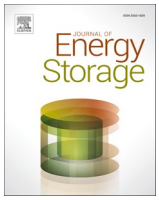
Journal of Energy Storage 116 (2025) 115901



Contents lists available at ScienceDirect

Journal of Energy Storage

journal homepage: www.elsevier.com/locate/est



Research papers



Green synthesis of carbon aerogels derived from rice husk for advanced supercapacitors

P. Atanasio [a], R.Y.S. Zampiva [a], A. Fornari [a], C. Mancini [a], A. Aurora [b], A.G. Marrani [c], M. Rossi [a,d], M. Pasquali [a,d], F.A. Scaramuzzo [a,d,*]

[a] Department of Basic and Applied Sciences for Engineering, SBAI, Sapienza University of Rome, Via A. Scarpa 14, 00161 Rome, Italy
[b] Department of Energy Technologies and Renewable Sources C.R. ENEA Casaccia, Via Anguillarese 301, 00123 Rome, Italy
[c] Department of Chemistry, Sapienza University of Rome, Piazzale A. Moro 5, 00185 Rome, Italy
[d] Research Center on Nanotechnologies Applied to Engineering of Sapienza, CNIS, Sapienza University of Rome, Piazzale A. Moro 5, 00185 Rome, Italy

ARTICLE INFO

Keywords:
Carbon aerogels
Rice husk
Supercapacitors
Nanomaterials
Energy storage
Waste-to-energy

ABSTRACT

In the perspective of a green transition, coupling the use of sustainable materials with the development of efficient energy conversion and storage systems is highly desirable. Within this context, the present study focuses on the exploitation of rice husk (RH), an abundant agricultural waste, for the synthesis of carbon aerogels (CAs) derived from cellulose, and their application in energy storage devices. The synthetic process shown here includes a two-step pre-treatment removing lignin, hemicellulose, and silica, followed by gelation, drying, and carbonization. Variations on the developed methodology are presented, evaluating their impact on morphology, structure, and electrochemical performances of the CAs. A broad variety of characterization techniques, including scanning electron microscopy, energy-dispersive X-ray spectroscopy, X-ray diffraction, Raman spectroscopy, X-ray tomography, FTIR, XPS, and Brunauer-Emmett-Teller analysis, has been used to elucidate their morphological and structural properties. The electrochemical performances assessed by cyclic voltammetry and galvanostatic cycling tests demonstrates that when used as electrodes in supercapacitors, some of the obtained CAs display exceptional stability, with a capacitance retention up to 81.2 % after 10,000 cycles. Even without exploiting the well-known synergistic effect observed for composite carbon-based electrodes, the life cycle and capacitance retention we obtained are comparable to those of pyrolytic carbon synthesized from RH in harsher conditions and other 3D cellulose-based composites described in the literature, which proves the robustness of our best pristine CA, and offers a promising perspective on green energy storage solutions.

1. Introduction

The worldwide energy demand is currently met at 80 % by fossil fuels [1]. Aiming to reduce fossil fuel consumption, the combination of sustainable energy technologies and green processes development for exploitation of secondary raw materials (i.e. industrial or agricultural wastes and biomasses) is currently gaining attention [2,3]. Sustainability cannot be separated from the development of efficient energy conversion [4,5] and storage systems, which includes design and fabrication of electrode materials [6–8], advancement of new generation technologies [9,10], and geometry optimization [11,12]. Characterization methods play a crucial role as well, providing information concerning the electrode surface and inner of the devices, even in situ and operando [13–15]. Being carbon and carbon-based materials widely exploited in electrochemical devices, biomasses represent virtuous eco-friendly starting matrices, due to their natural abundance, renewability and biodegradability [16]. Among the others, a promising and appealing biomass to be recycled and converted into high-value products is the outer covering of the rice kernel, i.e. rice husk (RH), which is mostly made of cellulose (≈38 % wt), lignin (≈22 % wt) and hemicellulose (≈18 % wt), and silica (≈20 % wt) [17]. RH has already been exploited as a starting material for the design and production of a variety of carbon-based micro- and nanostructures for energy applications, e.g. biochar, electrodes for lithium-ion batteries, capacitors and supercapacitors [18,19]. Focusing on the latter, it is worth notice that valuable electrodes for supercapacitors have been successfully fabricated by employing many different forms of carbon, such as graphene, graphene oxide and nanotubes, either pristine and in hybrid structures coupled with metals or other materials [20–22]. Besides the electrode materials,

* Corresponding author.
E-mail address: francesca.scaramuzzo@uniroma1.it (F.A. Scaramuzzo).

https://doi.org/10.1016/j.est.2025.115901
Received 1 July 2024; Received in revised form 23 January 2025; Accepted 16 February 2025
Available online 4 March 2025
2352-152X/© 2025 The Authors. Published by Elsevier Ltd. This is an open access article under the CC BY license (http://creativecommons.org/licenses/by/4.0/).

Abbreviations

RH	Rice Husk
CAs	Carbon Aerogels

the performances of the supercapacitors are highly affected by the electrolyte. In the literature either neutral, acid or alkaline aqueous solutions have been widely exploited, the most popular being based on Na_2SO_4, H_2SO_4, and KOH [23]. The advantage in the use of alkaline electrolyte is that OH^- ions' higher conductivity and ionic mobility can improve capacitive activity [24]. Among all the possible structures and combinations, carbon aerogels (CAs) are known as particularly effective, allowing the fabrication of electrodes with remarkable performances [25]. CAs can be obtained from different precursors, e.g. organic monomers, biomasses, polymers, graphene or carbon nanotubes. Regardless of the starting material, they are usually prepared in three steps, i.e. gelation, drying and carbonization [26]. Sol-gel synthesis is currently considered highly convenient, since it allows to obtain either pristine and composite nanomaterials for energy in a relatively easy way and high yields [27,28]. However, starting from biomasses the presence of lignin can affect the structural and functional features of the final product. When lignin is kept, potentially toxic organic solvents and harsh drying conditions can be necessary for the synthesis of the aerogel [29]. Removal of lignin can be performed with a variety of techniques [30], giving the possibility to perform gelification and subsequent drying of the residual cellulose in a greener environment [31]. The versatility of CAs is due to their outstanding physical and chemical properties like low density, chemical stability, high specific surface and a 3D porous structure, which led to their wide use in a broad variety of applications, ranging from mechanics to catalysis, electricity and heat transfer [32]. In a view of circular economy, here we present a successful use of RH to fabricate light, stable and highly conductive cellulose-based CAs, which showed excellent properties as electrodes for supercapacitors. Besides the three abovementioned conventional steps, the synthetic strategy we propose only includes a two-step pre-treatment with commercially available reactants. Variations in the methodology were investigated, elucidating the influence of pre-treatment conditions on the morphology and structural features. To the best of our knowledge, RH derived materials for supercapacitors and other energy storage devices normally includes pyrolytic hard carbons, but this waste has never been used to obtain CAs from purified cellulose [33]. The obtained CAs were tested as electrode materials in supercapacitors assembled in symmetric configuration, using 6 M KOH aqueous solution as electrolyte. The electrochemical characterization performed by cyclic voltammetry and galvanostatic cycling tests demonstrates that they can display exceptional stability, with a capacitance retention up to 81.2 % after 10,000 cycles. Despite the absolute capacitance values are lower than those of other electrodes, especially when synergistic effect of different components is exploited [34], the life cycle is longer and the capacitance retention is comparable to that of other 3D cellulose-based composites used in supercapacitors with similar electrolytes [35,36]. Moreover, a comparison with pyrolytic carbon-based electrodes from RH shows that we can obtain comparable performances with milder synthetic conditions [37]. The abovementioned considerations confirm the potentialities of recycled materials and highlight the robustness of our best pristine CA itself.

2. Materials and methods

2.1. Materials

RH was purchased by LD Carlson Co. and crushed in a fine powder before working. All the other reactants, i.e. sodium hydroxide (NaOH 98.5 %, CAS number 1310-73-2, Sigma-Aldrich), acetic acid (CH_3COOH 99–100 %, CAS number 64-19-7, 99–100 %, Sigma Aldrich), sodium chlorite ($NaClO_2$ 80 %, CAS number 7758-19-2, Sigma-Aldrich), potassium hydroxide (KOH 90 %, CAS number 1310-58-3, 90 %, Sigma-Aldrich), polyvinylidene difluoride (PVDF 100 %, CAS number 24937-79-9, Sigma-Aldrich), and urea (NH_2CONH_2 99–100 %, CAS number 57-13-6, Carlo Erba) were used as provided, without further purification.

2.2. RH pretreatment to obtain cellulose

RH underwent a two-step pretreatment to obtain pure cellulose. In the first step, the removal of the lignin and part of hemicellulose was performed by suspending the starting matrix in a 1.7 % wt sodium chlorite and 3.36 gL^{-1} acetic acid aqueous solution at 80 °C for 1 h under magnetic stirring (ratio: 1 g of solid in 17 mL of solution). The procedure was repeated for four times. After each time, the solid residue was filtered using qualitative filter paper, washed with distilled water till neutrality and dried in oven. In the second step, the removal of silica, other inorganic impurities and the remaining part of hemicellulose was performed by further digestion of the solid in NaOH 1 M (ratio: 1 g of solid in 8 mL of solution) for 1 h at reflux under magnetic stirring. The final residue was filtered using qualitative filter paper, washed with distilled water till neutrality and dried at 120 °C in oven to constant weight. The two steps were performed either in the abovementioned order (Route 1), or in reverse order (Route 2).

2.3. Cellulose gel and CA formation

The cellulose pulp obtained as previously described was dissolved into a 7 % wt NaOH and 12 % wt urea aqueous solution in ice bath to get a final concentration of either 2 % wt or 7 % wt of cellulose. After complete dissolution, the product was aged at 50 °C overnight, giving rise to the formation of a stable cellulose gel (i.e. a cohesive, gelificated cellulose-based structure). Regeneration was performed to remove the excess of base by replacing the supernatant with distilled water. The process was repeated until neutrality. Overall, 1.2 L of distilled water for each starting gram of cellulose was necessary. The thus regenerated gel was then freeze dried at −50 °C for 5 h and carbonized under Ar atmosphere at 800 °C for 2 h in a tubular furnace, finally giving the desired CA. Temperature and time for pyrolysis were chosen according to the literature, since it has been observed that pyrolysis at 800 °C usually produces optimized surface and pore distribution that maxims catalytic and electrode performances [38].

From now on, the different CAs fabricated for this work will be indicated as reported in Table 1, depending on the followed synthetic procedures.

2.4. Electrode preparation, cell assembly and post-mortem electrode recovery

Electrodes were fabricated by mixing CAs, PVDF and acetylene black (80:10:10) and tested in two-electrodes T-cells assembled in symmetrical configuration with KOH 6 M as electrolyte. For post-mortem characterization, cycled devices mounting 1B CA-based electrodes were disassembled, the electrodes were gently removed, rinsed with distilled water and dried in oven.

Table 1
Name and corresponding synthetic procedures of the samples used in this work.

Sample name	Cellulose extraction procedure	Cellulose concentration in gel
1A	Route 1	2 % wt
1B		7 % wt
2A	Route 2	2 % wt
2B		7 % wt

2.5. Characterization

Field emission scanning electron microscopy (FESEM) and energy dispersive X-ray Spectroscopy (EDX) were performed using a Zeiss Auriga electron microscope.

X-ray Diffraction analysis was performed using a Philips PW1830 APD3520 diffractometer using Cu-K_α radiation (λ 1.54 Å) in 2θ range 8–40°, with 40 kV voltage and 30 mA current.

Raman spectroscopy was performed with a Renishaw inVia Raman confocal Microscope using a green lamp (532.1 nm, output power 50 mW) and 100× lens, in the Raman Shift range 800–2200 cm^{-1}.

The porosity of the samples has been evaluated with a Quadrasorb SI instrument from Quantachrome, using N_2 as analysing gas at 77 k bath temperature. Brunauer Emmett Teller (BET) method allowed to obtain surface area, while pore volume has been obtained by using the density function theory (DFT) method.

X-ray tomography was performed using a 3D Sub-micron X-ray resolution microscope Zeiss Xradia Versa 610 both in absorption and phase contrast mode. For absorption experiments, 2401 projections were acquired with a 4× objective, 4 s of exposure time at 40 kV and 3 W, pixel size of 3.5 μm. For phase contrast measurements 2401 projections were acquired with a 20× objective, 80 s of exposure time at 40 kV and 3 W, pixel size of 0.7135 μm. Both experiment settings used air as filter for the X-rays. The reconstruction of dataset was performed using Zeiss Scout-and-Scan Control System Reconstructor, while 3D models of the samples were investigated and processed with software Dragonfly Pro from Object Research Systems (ORS).

Electrochemical performances were evaluated using a multichannel VMP potentiostat by Perkin Elmer Instruments. Galvanostatic cyclations and cyclic voltammetry tests were performed in −1.0–0.2 V potential window respectively at different currents (0.1–1.0 $A{\cdot}g^{-1}$) and potential scan rates (1–50 $mV{\cdot}s^{-1}$). Electrochemical impedance spectroscopy (EIS) was performed in potentiostatic condition (PEIS) at 0 V open cell voltage in a range of frequency 1 mHz–1 MHz with an amplitude of potential of 10 mV.

FTIR analysis was performed using a Bruker Lumos II micro-FTIR ATR equipped with Ge crystal with 4 cm^{-1} resolution and 2048 data points scan. Per each sample, 9 different spectra were acquired and mediated.

XPS measurements were carried out on 1B CA-based electrodes before and after cycling using an Omicron NanoTechnology Multiprobe MXPS system equipped with a monochromatic Al Kα ($h\nu = 1486.7$ eV) X-ray source (Omicron XM-1000), operating the anode at 14 kV and 16 mA. For the measurement, the samples were attached via a double-sided conductive scotch tape to the XPS sample holder. The C 1s photoionization region was acquired using an analyzer pass energy of 20 eV. A take-off angle of 21° with respect to the sample surface normal was adopted. The experimental spectra were theoretically reconstructed by fitting the secondary electrons background to a Shirley function and the elastic peaks to pseudo-Voigt functions described by a common set of parameters: position, full-width at half-maximum (FWHM), Gaussian-Lorentzian ratio.

3. Results and discussion

The two different procedures followed for synthesizing carbon aerogel from rice husk are summarized in Fig. 1. The starting raw matrix was treated with a two-step pre-treatment in which bleaching process with sodium chlorite in acidic environment allowed to dissolve the lignin part, making the matrix appear white, while silica and part of hemicellulose were removed by sodium hydroxide. The two steps were performed in sequence either starting from lignin removal (Route 1) or silica removal (Route 2) in order to identify possible differences of the final products in terms of morphology, structure and electrochemical performances. The final yield of cellulose calculated by gravimetric measurements before and after each process was around 33 % with Route 1 (i.e. (i) $NaClO_2$, (ii) NaOH), and around 37 % when following Route 2 (i.e. (i) NaOH, (ii) $NaClO_2$). Both these values are in good agreement with the RH content of cellulose reported in literature [17].

The obtained cellulose was rapidly dissolved in the basic gelification solution, forming a dark yellow liquid in which, during the aging process, fibres reorder forming an interconnected hydrogel containing sodium hydroxide and urea. The regeneration necessary to exchange the solvent was considered complete when the surfactant got neutral pH and the gel turned from dark yellow to white. After freeze drying, the interconnected cellulose structure was transformed into an ordered

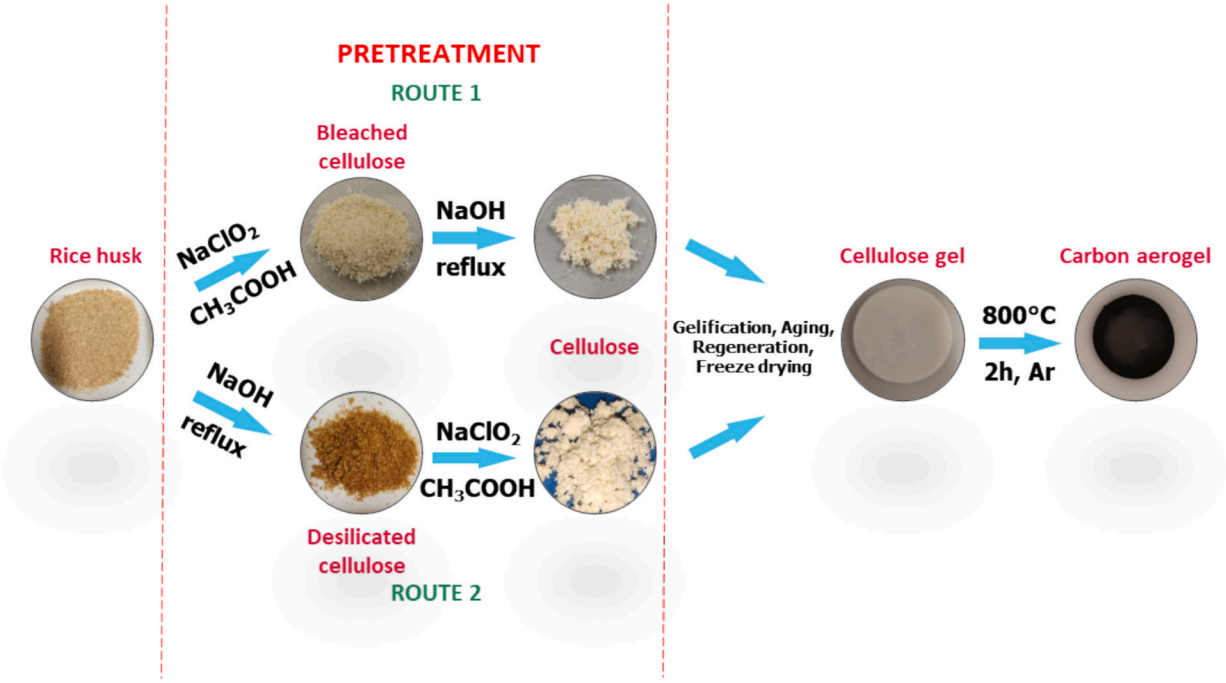


Fig. 1. Different preparation procedures to obtain CAs starting from RH.

matrix of carbon fibres by mean of carbonization. During this step, the organic and volatile components are removed by degradation and evaporation, while the residual material becomes a high conductive aerogel. The yield, volume shrinkage, and final density of the 4 different CAs obtained upon combination of the two different pre-treatment pathways and the two different cellulose concentrations for gel formation are shown in Table 2. Since the gel formation and drying were performed in cylindrical shaped beakers, the volume was calculated by simply considering average diameter and height of cellulose gel and CAs. Apparently, higher cellulose concentration results in higher CA yield with lower volume shrinkage and densities. On the other hand, a comparison of samples obtained by using the same cellulose concentration, but different synthetic pathways shows that Route 2 results in higher shrinkage and density. The obtained densities are in good agreement with experimental values and equations reported in literature for aerogels obtained with comparable cellulose concentrations [39].

Morphology, dimension, and elemental distribution of samples were investigated by mean of SEM-EDX. Typical SEM micrographs of RH and all the intermediate steps are shown in Supplementary Information (Fig. SI 1–Fig. SI 5). In Fig. 2 typical micrographs obtained for the 4 different kinds of final samples at low magnification are reported. All the samples show a rather similar general morphology, characterized by interconnected networks of both fibres and sheet-like platelets made of compacted structures of carbonized cellulose. No significant differences in the relative distribution of these two microstructures can be observed. Using the software Image J, a statistical analysis of the fibre dimensions was performed, considering at least two hundred fibres per each sample. All the measured diameters are in the range 2–6 μm and the average values are between 3.3 and 4 μm, the lowest average value being the one of 1B (see inserts in Fig. 2). At first glance, the average values decrease upon increasing the concentration of cellulose in gels and decrease moving from Route 1 to Route 2. However, the standard deviation values suggest that the different average diameter values might not actually indicate meaningful differences in the samples.

Despite the comparable general morphology, SEM analysis at higher magnification (Fig. 3) shows that the surface of samples 1A and 1B (i.e. obtained following Route 1) looks rougher, with clusters of carbon nanostructures and pores all over fibres and platelets, which seem to get bigger and more agglomerated at higher concentration of cellulose. On the other hand, the surfaces of samples 2A and 2B (i.e. obtained with Route 2) appear cleaner. At first glance, the surface of 2B might seem smoother than the surface of 2A, but the difference is definitely less remarkable than in the previous case.

Fig. 4 shows the results of EDX analysis, providing the elemental composition of the materials obtained after each step. The shown values were obtained by using at least two samples per step and averaging at least three measurements for each sample. RH is naturally rich in silicon (as SiO_2) and contains mostly cellulose, hemicellulose and lignin [18]. In Route 1 the first step removes lignin and part of the hemicellulose but not silica and cellulose, thus increasing the percentage of silicon in the samples. The second step aims to purify the samples by means of NaOH for the upcoming gelification process, removing the silica and the remaining part of hemicellulose, and leaving just the cellulose. As expected, no silicon is present in the sample after this treatment. On the other hand, in Route 2 the first step is the removal of silica with NaOH. As shown in Fig. 4, such removal is totally effective, even though the samples still contain a remarkable amount of hemicellulose and lignin. Consequently, in order to purify cellulose, they must be treated with $NaClO_2$ in acid environment. Whatever the followed pre-treatment route is, once obtained pure cellulose, the synthesis including gelification, aging, freeze drying, and carbonization results in samples with comparable elemental composition in terms of C and O %wt.

The high temperature carbonization performed in Ar atmosphere allows to remove the volatile and side-reactions components, leading to the formation of a material with low oxygen content, high C—C double bonds percentage and a disordered graphite structure. A residual and negligible (below 1 %) silicon percentage has been observed in some of the final products.

XRD was used to investigate the structure of the samples, also monitoring possible changes during the synthetic process. The obtained results are shown in Fig. 5. RH spectrum clearly shows the pattern of cellulose I_β, with a main peak at around 22° corresponding to plane (200), two peaks at around 16° for (110) and (1–10) planes and a third smaller peak at 34° for (004) plane [40]. It is worth notice that RH contains also other components, which are not detectable here because of their amorphous nature.

For each sample, crystallinity index (CI) has been calculated according to Eq. (1):

$$CI = \frac{I_{200} - I_{am}}{I_{200}} \quad (1)$$

where I_{200} is the intensity of the main peak of I_β cellulose and I_{am} is the minimum intensity between (110) and (200) peaks, which accounts for the cellulose amorphous component [41]. The obtained results are shown in Table 3. Even if these values are not representative of the real crystallinity percentage, they can be useful to give an estimation of each sample's evolution during the CA synthesis. The crystallinity of cellulose in raw RH is around 27.08 %, reasonably low because of the presence of other components in the matrix.

As clearly visible in Fig. 5, whatever route is followed the structure of cellulose I_β is maintained in the first two steps, with an increase of the crystallinity index up to 52.24 % for Route 1 and 53.18 % for Route 2, due to the progressive removal of amorphous components of RH. It is well known that NaOH is able to induce crystalline transition from cellulose I_β to cellulose II (i.e. mercerization process). However, this is not our case during the desilication step, probably because of the high dilution experimental conditions. Being the values of crystalline index very similar, apparently there is no effect of the RH pre-treatment route on the structural features of the purified cellulose samples.

In both the synthetic procedures, NaOH swells the fibres while urea brings them in solution, thus breaking the crystalline clusters and destroying long range order. In this case a transition from cellulose I_β to cellulose II can actually be observed [40]. When the gel is formed, cellulose fibrils arrange in different structures and the typical peaks of cellulose I_β disappear due to cellulose mercerization causing chains moving from parallel to antiparallel configuration. In fact, cellulose gel diffractograms broaden and show less intense signals, which indicates an increasing of the percentage of amorphous material. The residual weak peaks at values of 2θ around 12°, 20° and 21.5° can be assigned respectively to (1–10), (110) and (200) planes of cellulose II, which is obtained upon conversion of cellulose I_β in high concentration base environment, as expected. As qualitatively suggested by the diffractograms shape commented above, the crystallinity indexes calculated by using Eq. (1) show very low values. Finally, carbonization process induces the transformation of cellulose fibrils and clusters into the graphitic structure of carbon aerogels. All peaks of cellulose disappear, and in the examined range only the main peak of carbon (002) is visible. This peak, characterized by low intensity and very broad shape, indicates the partial graphitic nature of the obtained CAs. The peak of CAs obtained with Route 1 is centred around 23.9°, while the peak of CAs obtained with Route 2 CAs is centred around 24.5°, which indicates a

Table 2
Final yield, volume shrinkage and density of the four different obtained CAs.

Sample	Yield %	Volume shrinkage %	Density ($mgcm^{-3}$)
1A	4.92 %	73.64 %	44.7
2A	3.22 %	84.04 %	51.6
1B	5.22 %	58.23 %	41.4
2B	5.94 %	61.71 %	43.5

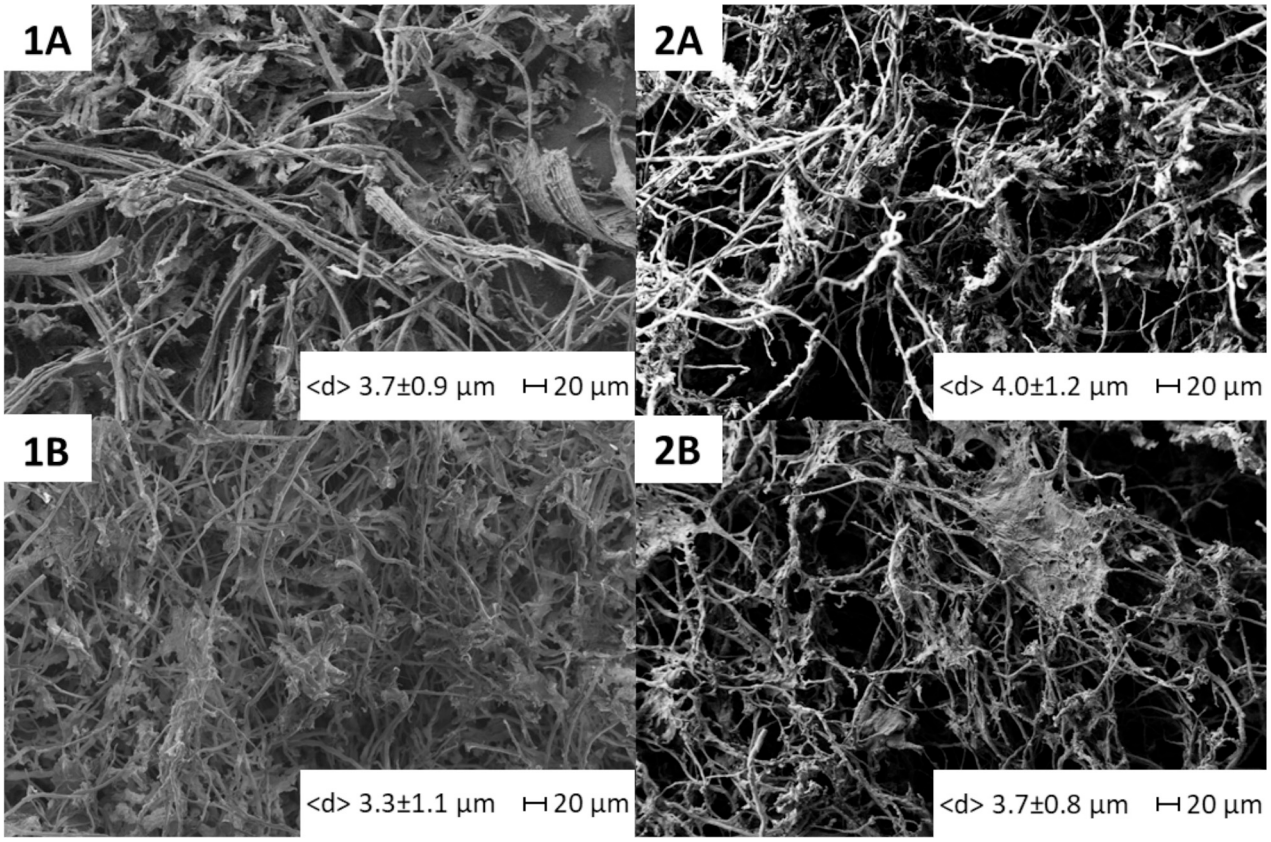


Fig. 2. Wide panoramic SEM images (500× magnification) of the four types of CAs produced. Average diameter of fibres is indicated on each image.

plane distance of 3.7 Å and 3.6 Å respectively. Therefore, we suggest that the two different synthetic routes induce a minor but clear difference in the crystalline structure of the final products.

The graphitic nature and the disordered components of CAs were investigated by means of Raman spectroscopy. In Fig. 6 the obtained spectra are shown. The Raman shift, intensity and shape of the two main graphite peaks, i.e. D-band, which is representative of defects and disorder in the carbonaceous structure, and G-band, that is due to interlayer vibration of graphite planes, are similar for all samples.

I_d/I_g ratios for all the CAs are shown in Table 4. Samples obtained at 7 % wt cellulose concentration have both ratio equal to 0.91, while samples obtained at 2 % wt show higher variability, having I_d/I_g ratio 0.89 and 0.97 for 1B and 2B respectively. However, these differences are almost negligible, and all the calculated values suggest that the samples have the features of disordered graphitic materials, characterized by structural defects and a reasonable conductivity.

BET analysis allowed to obtain the specific surface area (SSA), while pore volume and pore width have been obtained by using the density function theory (DFT) method. The results for all the as prepared CAs are shown in Fig. 7 and summarized in Table 5. It is worth notice that DFT has been preferred to BJH, being considered more reliable for micro- and mesopores, and recommended by The International Standard Organization (ISO) for this purpose [42]. Samples 1A and 2B offer a very small surface area and their pore width is 4.08 nm and 3.68 nm respectively. As it is possible to observe in Fig. 7, both the samples have a large amount of mesopores that hinders the formation of a wide surface area. Moreover, the pore width shows high variability, with a broad distribution of the dimensions. In the case of samples 1B the SSA value is equal to 341.73 m^2g^{-1}, which might seem considerably smaller than sample 2A, which on the opposite shows the considerable value of 728.30 m^2g^{-1}, the biggest of the four CAs. However, sample 2A pore volume is almost totally ascribable to micropores: actually, the pores having width around 1.14 nm seems to account for more than the 80 % of the total pore volume. On the other hand, samples 1B, despite having a smaller SSA and a smaller average diameter, shows a pore width distribution which seems much richer in mesopores. This can actually represent an optimum compromise between high surface area and hierarchical porous structure and can enhance the performances of CAs-based electrodes, offering both wide surface area for charge accumulation processes and larger pores as channels for ion diffusion in the carbonaceous electrode. As reported in literature, interconnected meso- and macropores can provide fast ion channels thus facilitating ion transport for high performance supercapacitors [43].

To characterize the whole bulk samples, and not exclusively their surface, we performed X-Ray Tomography observations on both the entire vertical direction of the samples and their internal core using absorption and phase contrast modes respectively. Tomography has already been successfully applied in the study of materials in energy applications showing huge potentialities in the investigation and characterization of such materials [13,14]. This technique allows to observe a cylindrical portion of CAs, analysing slices of samples in vertical direction, i.e. along Z axis which goes from the bottom to the top of the samples, but also in horizontal direction, i.e. along Y or X axis, which are equivalent thanks to the cylindrical symmetry of samples. Length, width and distribution of the carbonaceous structures are the main parameters that we were able to analyse. Fig. 8 shows the vertical distribution of the network within the samples both in absorption and in phase contrast mode. A 3D scheme in the upper left part of each image indicates the portion of sample observed. The brighter portions of the 2D figures are the portions of sample with higher mass density to the X rays and therefore they have been identified as the platelets formed by fibres. Samples obtained at 2 % concentration of cellulose (i.e. 1A and 2A) show higher density of platelets at their bottom. Comparing the two samples, 1A platelets appear smaller than 2A platelets, this difference being especially enhanced in the lower extreme part. On the other hand, samples at 7 % cellulose concentration (i.e. 1B and 2B) show a more

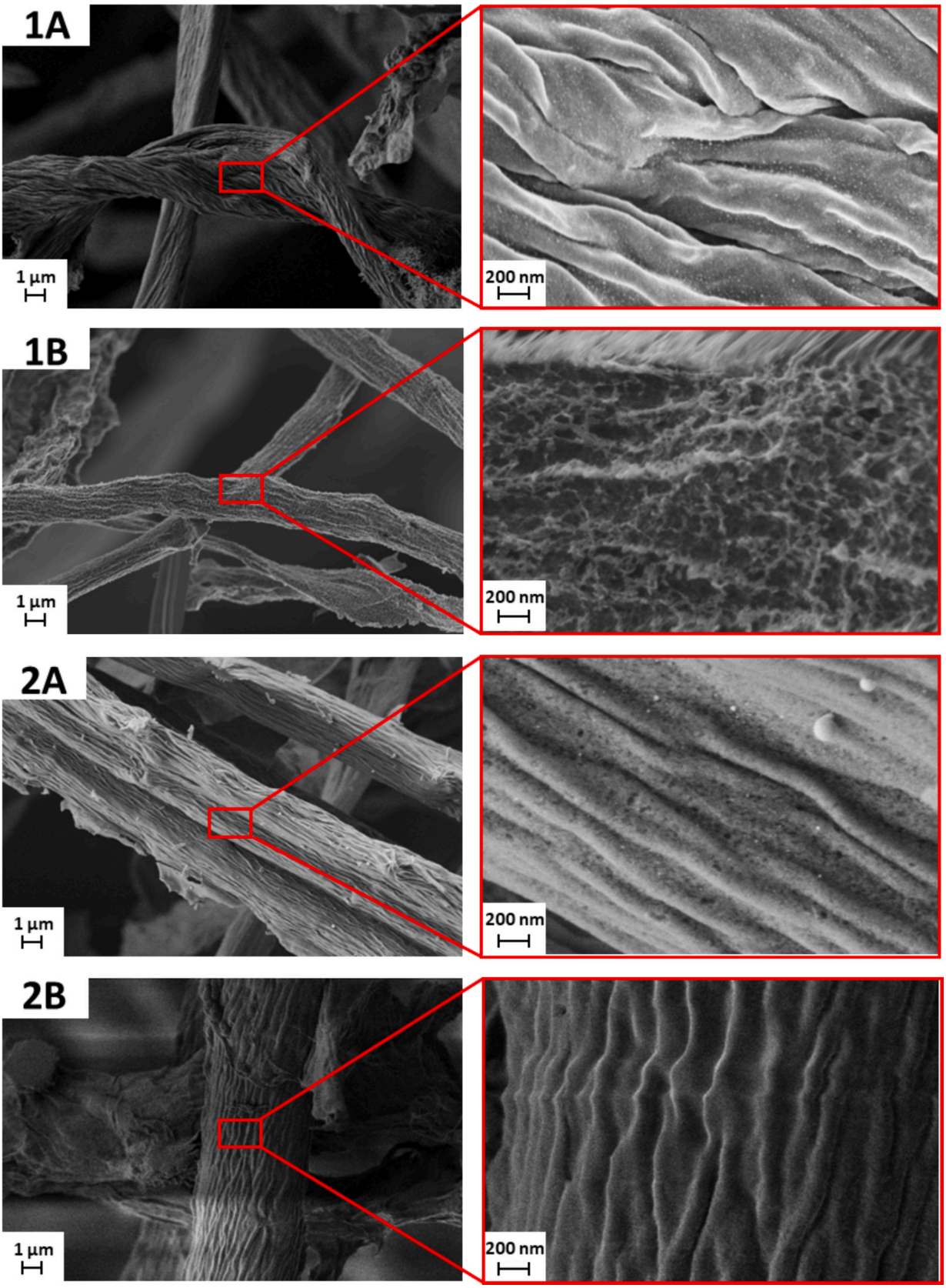


Fig. 3. SEM images (10k× magnification) of the four types of CAs produced, and corresponding 50k× magnification of selected areas.

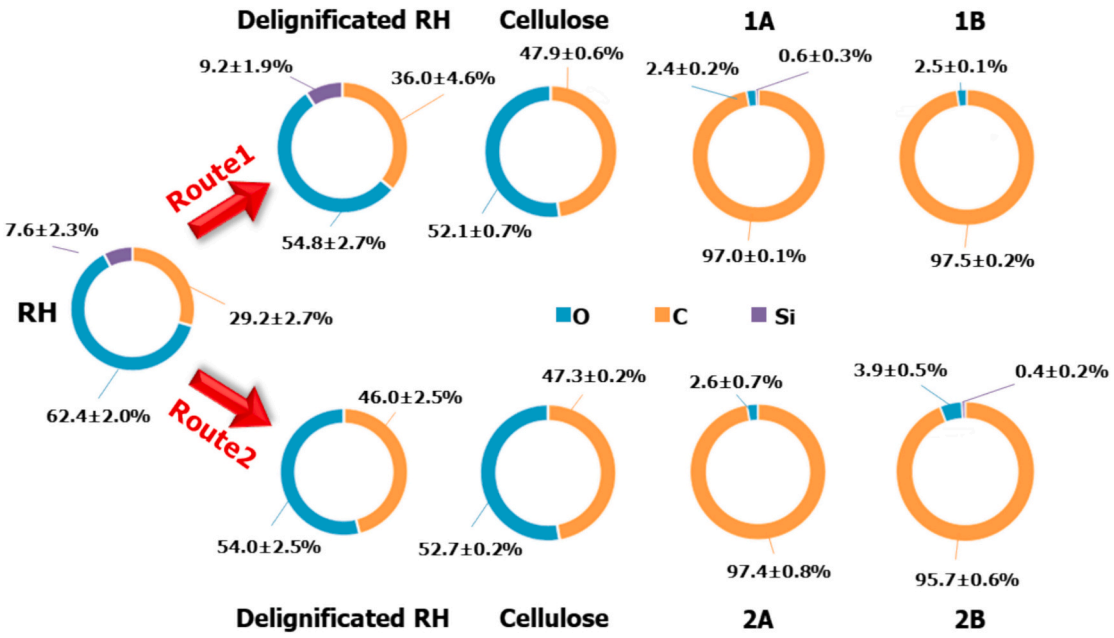


Fig. 4. Typical EDX elemental analysis (*w*/w%) of the materials obtained after each step.

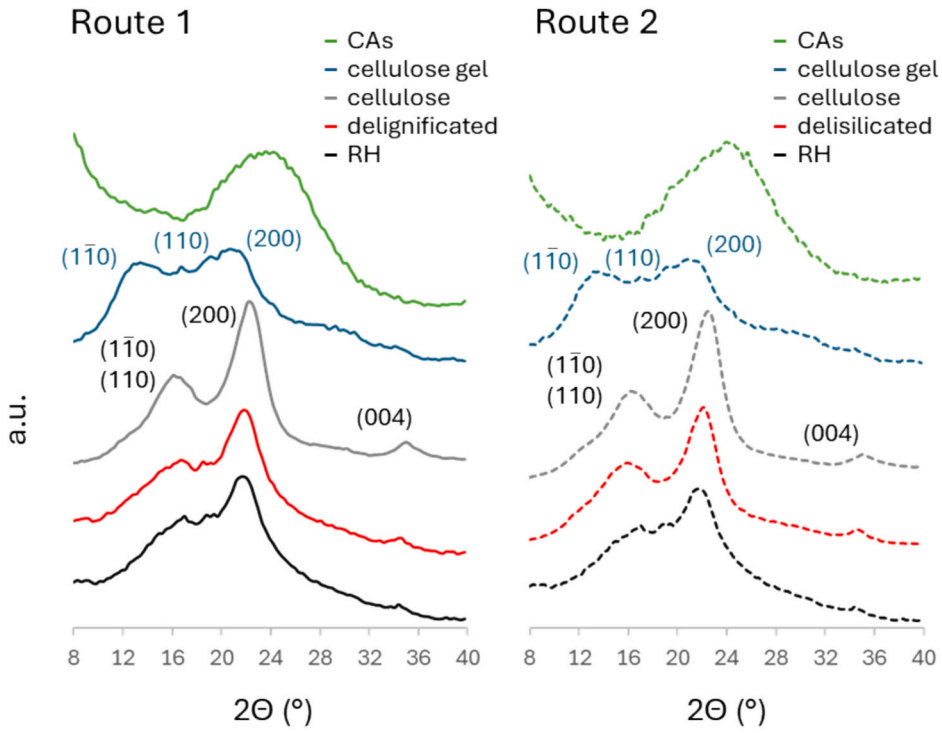


Fig. 5. XRD spectra showing the evolution of the crystalline structure of samples respectively during synthetic Route 1 (left) and Route 2 (right). Miller indexes of cellulose I_β, cellulose II and carbon peaks are reported respectively in black, in blue, and in red. (For interpretation of the references to colour in this figure legend, the reader is referred to the web version of this article.)

homogeneous distribution of platelets in the vertical direction, and during carbonization the cellulose fibres tend to aggregate in the same way all over the samples. This experimental observation seems to be coherent with the behaviour of the samples at 2 % concentration of cellulose, which tend to compact, thus showing higher shrinkage and density.

Analysis in phase contrast mode allows to observe a smaller portion of samples compared to absorption mode. However, the resolution is highly improved, and the dimension of the platelets can be measured. Samples obtained following Route 1 show a lower density of platelets than samples obtained with Route 2. Following Route 1, the length of fibres increases with the cellulose concentration, going from 59.8 ± 4.9 μm in 1A to 120.6 ± 18.4 μm in 1B. On the other hand, platelets width slightly decreases, going from 6.7 ± 0.4 μm to 5.7 ± 0.6 μm. Therefore, following Route 1 at higher concentration of cellulose (i.e. sample 1B) we can observe a lower amount but longer and thinner platelets, with a tendency to form elongated aggregates and fibrotic structures.

Compared to samples obtained with Route 1, samples obtained with

Table 3
Crystallinity Index of RH and cellulose samples calculated according to Eq. (1).

	Sample	Crystallinity Index
	Rice Husk	27.08 %
Route 1	Bleached RH	31.39 %
	Cellulose	52.24 %
	Cellulose Gel	15.49 %
Route 2	Desilicated RH	42.19 %
	Cellulose	53.18 %
	Cellulose Gel	10.32 %

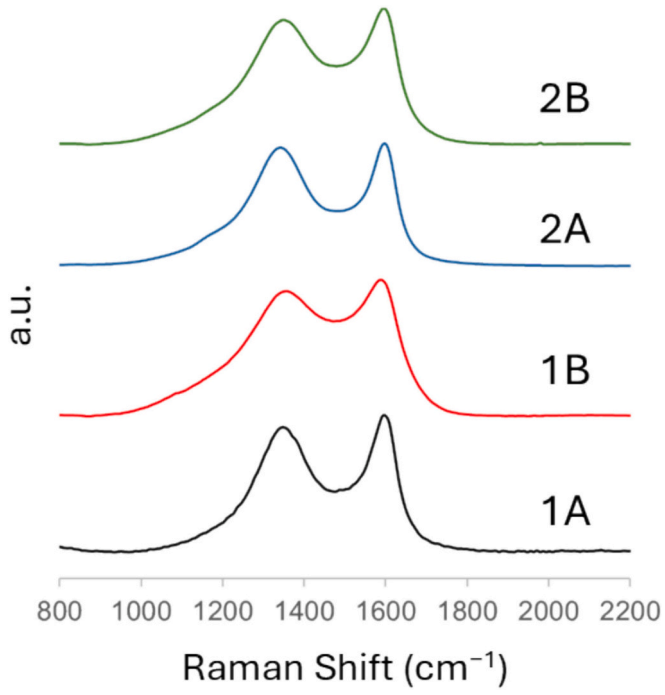


Fig. 6. Raman spectra of the four different CAs.

Table 4
Intensity ratio of D and G band for the four different CAs.

Sample	I_d/I_g
1A	0.89
2A	0.91
1B	0.97
2B	0.91

Route 2 show a remarkable number of platelets, characterized by higher average dimensions. As for samples obtained with Route 1, upon increasing the cellulose concentration they do not seem to undergo significant variations in terms of platelets distribution, while overall the samples tend to become more fibrotic, with visible variations in platelets shape and dimensions. In detail, sample 2A is characterized not only by elongated structures, but also by cluster-like platelets and three-dimensional aggregates. Differently from what observed in samples obtained with Route 1, both the average length of fibres and the average width of platelets decrease upon increasing the cellulose concentration, going respectively from around 114.7 ± 13.8 μm and 27.4 ± 8.1 μm in sample 2A to 92.3 ± 8.7 μm and 6.8 ± 0.3 μm in sample 2B. While the analysis along Z is rather informative, the structure of CAs along the horizontal direction shows that there are no significant changes in samples along the direction radial to the cellulose deposition during the formation of gel (Supplementary Information, Fig. SI 6).

The properties of the obtained CAs as electrodes in supercapacitors were investigated. Cyclic voltammetries collected for all the CAs at fixed scan rate (5 mVs^{-1}) are shown in Fig. 9A. All the curves show a quasi-rectangular shape, but the curves of samples synthesized with Route 1 have a larger area than those of samples synthesized with Route 2.

Upon increasing the scan rate, the curves start to lose their quasi-rectangular shape, and the current grows at higher potential, as shown for sample 1B in Fig. 9B. Electrochemical tests for all the studied electrodes are shown in Supplementary Information (Fig. SI 7).

Cyclic voltammetries allowed to calculate the materials specific capacitance using the formula:

$$C = \frac{\int IdV}{\varepsilon m V} \tag{2}$$

where C is the specific capacitance, I is the current, V is the potential window, m is the mass of the active material in the electrode and ε is the scan rate used in the experiment.

As reported in Fig. 9C, the capacitance tends to decrease upon increasing the scan rate, moving from 70.3 Fg^{-1} at 1 mVs^{-1} to 20.3 Fg^{-1} at 50 mVs^{-1}.

Within the same synthetic Route, the curve area is larger for CAs obtained from cellulose gel at higher concentration (Table 6).

Obtained capacitance is comparable to the one of pyrolytic carbon-based electrodes from RH [37], but lower than the one obtained for pure nanocellulose CAs by Zu et al. [44]. However, this is reasonable considering that our process brings to the formation of microcellulose, while the authors were using pure nanocrystalline cellulose, which implies larger surface areas and well-developed porous structures.

These results suggest that the sample with the better performance in terms of capacitance is sample 1B, which has a surface area of 341.73 m^2g^{-1} (an intermediate value among all the CAs), while samples with very low surface area like 1A and 2B show poor capacitance values. Surprisingly the lowest value of capacitance is given by sample 2A, which has the highest values of surface area and pore volume beneath our samples (see Table 5). Even if at first glance this experimental evidence might seem counterintuitive, it is actually in good agreement with some results already reported in literature and can be explained by considering that despite having the highest surface area, sample 2A is characterized by a really narrow pore distribution [45]. As pointed out in Fig. 7 and discussed above, all pores seem to be micropores with medium diameter around 1.14 nm, and in cases like this, i.e. when the totality of this surface area is ascribed to micropores with almost total absence of mesopores, the real surface available to the electrolyte is actually lower. Consequently, sample 2A could be unable to provide enough space for ions to diffuse inside carbon aerogel structure. Since the interphase between aerogel and the solution is connected to the charge accumulation, this limits the performance of 2A as electrode. On the contrary, sample 1B, offering an intermediate value of surface area, with a large portion of micropores (average diameter around 0.97 nm), has a more hybrid composition of micropores and mesopores, in particular around 5 nm. This hierarchical structure mitigates the diffusional limits of micropores and makes the surface reachable for electrolyte. An ion-accessible surface leads to more efficient charge storage, and this can explain the obtained electrochemical results.

Galvanostatic cyclations were used to evaluate performances and life of the electrodes. Capacitance has been calculated by:

$$C = \frac{i\Delta t}{mV} \tag{3}$$

where C is the specific capacitance, I is the constant discharging current density, Δt is the discharging time, m is the mass of active material in the electrode and V is the potential window in the galvanostatic discharge curves. The plots obtained (Fig. 10A) exhibit a triangular shape for all the samples with the same trend shown by CV curves, i.e. with 1B lasting for a longer time and having higher specific capacitance than the other

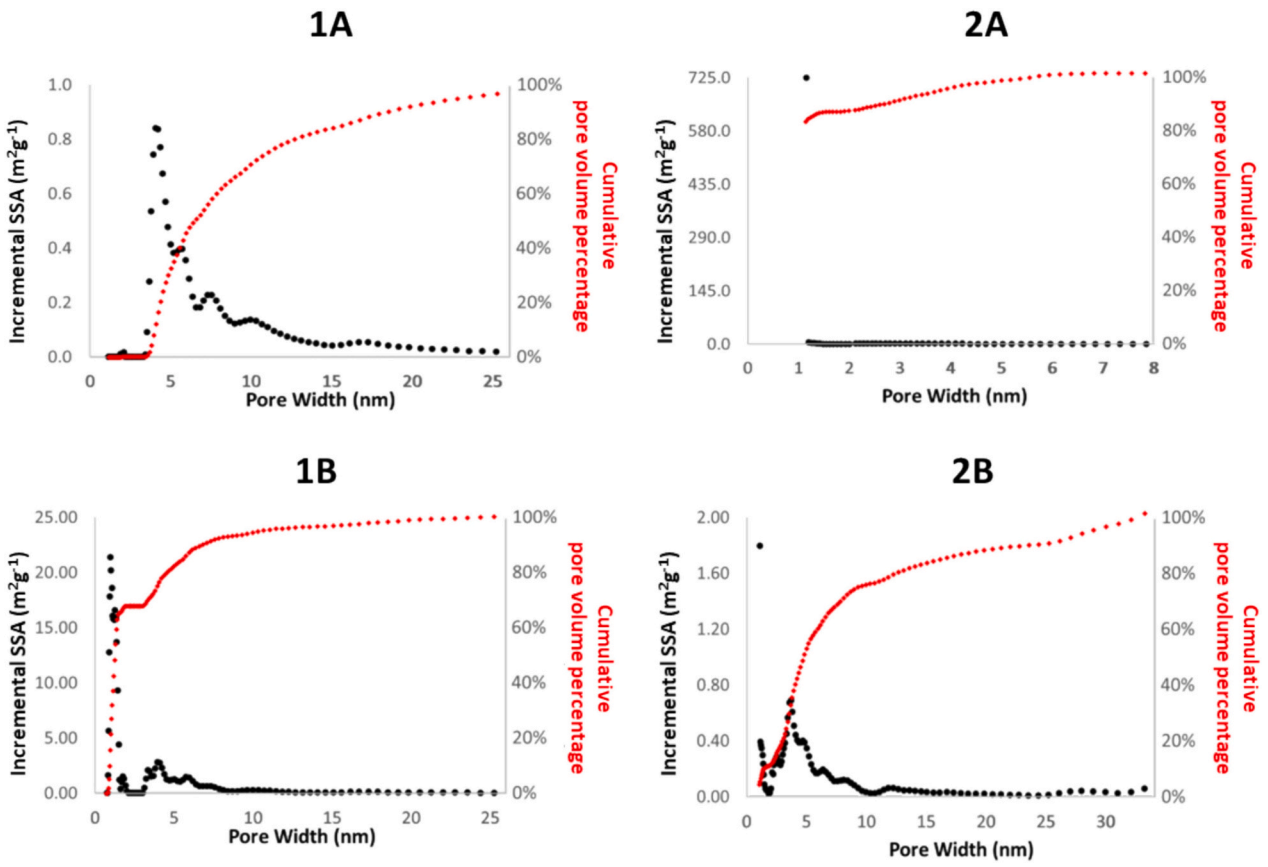


Fig. 7. Distribution of the contribute of pores to the final specific surface area for every sample (black curves) and cumulative pore volume (red curves). (For interpretation of the references to colour in this figure legend, the reader is referred to the web version of this article.)

Table 5
Values of specific surface area (SSA) obtained by BET, pore volume and pore width obtained by DFT analysis on the four samples.

Sample	SSA [m^2g^{-1}]	Pore volume [cm^3g^{-1}]	Pore width [nm]
1A	15.08	0.23	4.08
2A	728.30	3.21	1.14
1B	341.73	1.93	0.97
2B	22.79	0.24	3.68

samples (Table 7). Being the most promising, the electrochemical behaviour of sample 1B has been further investigated. As clearly shown in Fig. 10B–C, its capacitance decreases upon current increasing from 58.0 Fg^{-1} at 0.1 Ag^{-1} to 21.3 Fg^{-1} at 1 Ag^{-1}. The material exhibits good rate capability, returning to the original capacitance obtained at lower current even after increasing current up to ten times, thus indicating high stability of the electrodes under stress conditions (Fig. 10D).

Moreover, as shown in Fig. 11, it has an extraordinary long-life cycle. As clearly visible especially in the magnification chart, upon cycling the sample capacitance shows an initial increase, which is typical of all our samples, up to 75 Fg^{-1} after 200 cycles. Subsequently, the sample undergoes a noticeable loss of capacitance till around 500 cycles, when it starts to stabilize, thus experiencing a rather stable trend. The extreme robustness of the electrode is demonstrated upon comparing the capacitance values over cycling, which is around 58 Fg^{-1} after 1000 cycles and 47.8 Fg^{-1} after 10,000 cycles: overall, after 10,000 cycles the electrode shows a capacitance retention of 63 % compared to the maximum value, and an even more remarkable retention of 81.2 % compared to the value at 500 cycles.

To better describe how the polarization and the overall electrochemical behaviour of 1B CA-based electrode change over cycling, the shape of charge-discharge potential curves at various cycles have been reported in Fig. 12. Up to around cycle 200, the shape of the curves is maintained almost triangular with a low Irreversible drop (around 50 mV) between charge and discharge curves, while the duration of cycles increases, determining the enhancement of capacitance already commented above. After this, a decrease in capacitance is observed, with cycles becoming shorter in duration. At the same time, the quasi-triangular shape almost gets lost especially during charge, and the irreversible drop increases, reaching 100 mV around cycle 500 and going up to almost 300 mV after 10,000 cycles. During the whole process, the irreversible drop at beginning of charge increases too, keeping anyway below 200 mV in the range 0.2 V–0 V after 10,000 cycles.

The mechanism of self-discharge of 1B CA-based electrode has been studied. To this aim, after a charge at 0.1 Ag^{-1} down to −1 V, the electrode was left at open cell voltage and potential was recorded. As observable in the plot reported in Fig. 13, when the capacitor is disconnected it starts losing charges because of its internal resistance and there is an initial drop up to above −0.8 V. After this quick rise, the curve slowly becomes less sharp, only after 1 h reaching −0.3 V. From this point on the potential starts decreasing very slowly, and the initial open cell voltage around 0 V, being a symmetric cell, is reached after more than 20 h. Such a curve is in good agreement with general behaviour of supercapacitors, where three mechanisms of self-discharge usually appear, namely leakage current, faradic reaction and charge distribution [46]. The trend in Fig. 13 seems to be dominated by the initial sharp rise, due to charge distribution, the potential loss induced by charges not having sufficient time to distribute homogeneously in pores. On the other hand, the subsequent constant low slope increase seems due to leakage current. However, the short transition between these two behaviours might be affected by a mixed control phase in which the tiny amount of oxygen groups on the surface might be

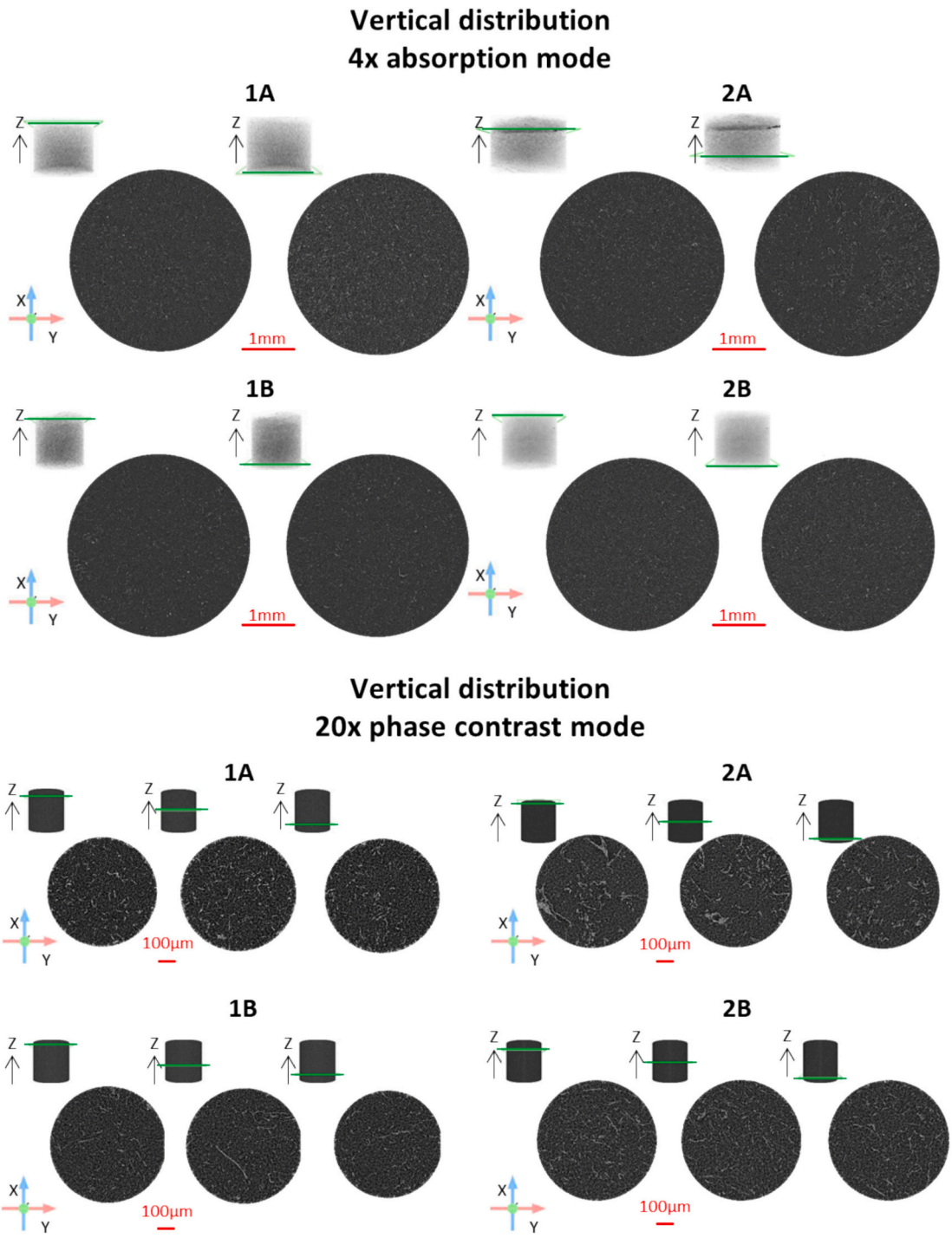


Fig. 8. X-Ray Tomography of all CAs samples obtained both in absorption mode (two images per sample, top panel) and in phase contrast mode (three images per sample, bottom panel). Each set of images shows a different slice of sample along the vertical Z axis as shown in the 3D model in the upper left corner of every slice.

responsible for faradic reactions potential lost during self-discharge. All the abovementioned considerations suggest that the mechanism is mainly driven by the initial charge distribution and the final leakage of current. This behaviour might be improved by controlling oxygen rich groups along surface, which affect both faradic reactions and leakage in carbonaceous materials, by applying slower charging current and higher holding time after charge [47]. Moreover, keeping in mind the needs for meso- and macropores interconnection to facilitate ion transport [43], it must be also taken into account that smaller pores lead to bigger resistances in charge distribution, and finding a compromise between different instances can be a reasonable way to optimize the material structure and optimize the design of the devices.

Additional information concerning the features of 1B CA-based electrode has been provided by Electronic impedance spectroscopy (EIS), whose results are shown in Supplementary Information (Fig. SI 8) along with the equivalent circuit used to fit data. The collected measurements show two main semicircles convoluted into a single one, similar to that observed in other carbonaceous materials by Cai et al. [48]. Sample 1B shows low resistances value, with series resistance only around 0.38 Ω and a low charge transfer around 2.28 Ω, while the third resistance component has been identified, as in Ref. 48, with a leak resistance of 0.8 Ω. These low values, in good agreement with other

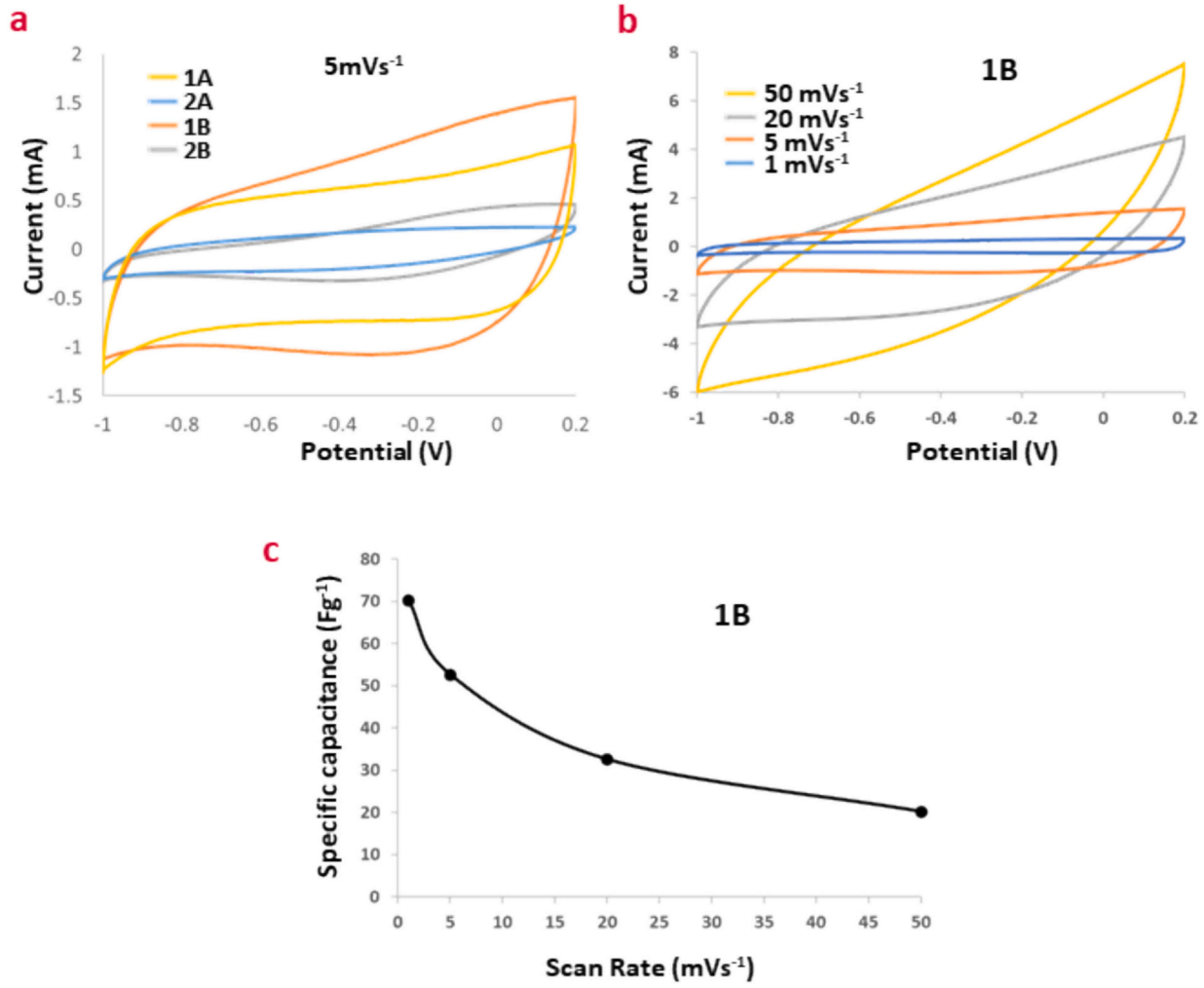


Fig. 9. A) cyclic voltammetry of different CAs samples at 5 mVs^{-1}, B) cyclic voltammetry of 1B CA at different scan rates, C) specific capacitance calculated from cyclic voltammetry of 1B CA at different scan rates.

Table 6
Capacitance calculated according to Eq. (2) by cyclic voltammetry performed at 5 mVs^{-1}.

Sample	Capacitance Fg^{-1}	Sample	Capacitance Fg^{-1}
1A	42.5	2A	12.6
1B	52.7	2B	13.7

literature EIS investigation over supercapacitors [49], demonstrate high conductivity along the framework, and the initial vertical trend of the Warburg region at lower frequency, with its vertical slope in the first values, indicates low resistance to electrolyte diffusion.

Stability of morphology and structure of 1B CA-based electrode has been investigated upon comparing SEM, FT-IR, and XPS of the pristine and the cycled material after a thousand cycles. SEM micrographs (Fig. 14) revealed that the surface of the pristine electrode actually seems made of short fibrotic elements surrounded and held together by a compact matrix of smaller structures, both particles and fibres, that ensures contact and electron conductivities through the electrode material (Fig. 14 a, b). Being composed by the electrode mixture (active material, adjuvant and binder), such matrix assures active surface for charge accumulation and reactions and also guarantees the charge conduction along the surface. After a thousand cycles, despite showing larger fibrotic structures due to electrode separator that remained attached to the electrode after disassembling the cells, the surface appears less covered by the smaller particles that densely composed the pristine surface (Fig. 14 c, d). Apparently, cycling induced the detachment of the smaller structures from the electrode matrix surface, thus leading to the loss of active material in the electrochemical solution and the decline of conductivity of electrons through the disordered graphitic domains. Such detachment could be due either to a low contact and cohesion between the electrode components or to the highly concentrated alkaline electrolyte used, i.e. KOH 6 M.

FTIR and XPS measurements were run on 1B CA-based pristine and cycled electrodes in order to characterize their chemical composition and the possible effects exerted by the electrochemical cycling. FTIR of the pristine electrode shows the typical signals of the CA as we already reported in our previous work [19], together with the peaks of PVDF at 1396 cm^{-1} (C—H), 1175 cm^{-1} (C—F), 612 cm^{-1} (C—F_2) [50]. After cycling, residual KOH appears [51] (Fig. SI 9).

As far as XPS is concerned, in good agreement with FTIR, in both samples the characteristic signals from C, O and F were detected (Fig. SI 10), this latter due to the PVDF binder used to prepare the electrode. Additionally, in the cycled electrode (Fig. SI 10 b) weak residual K and Si features were also present, the former deriving from the electrolyte and the latter from the glass-fibre separator. Finer details can be gained analysing via curve-fitting the high-resolution C 1s ionization regions (Fig. 15). In both cases, a predominant peak can be identified at low binding energy (BE) falling at 284.25 eV (Fig. 15, red curves) and with an asymmetric shape towards high BEs. According to the

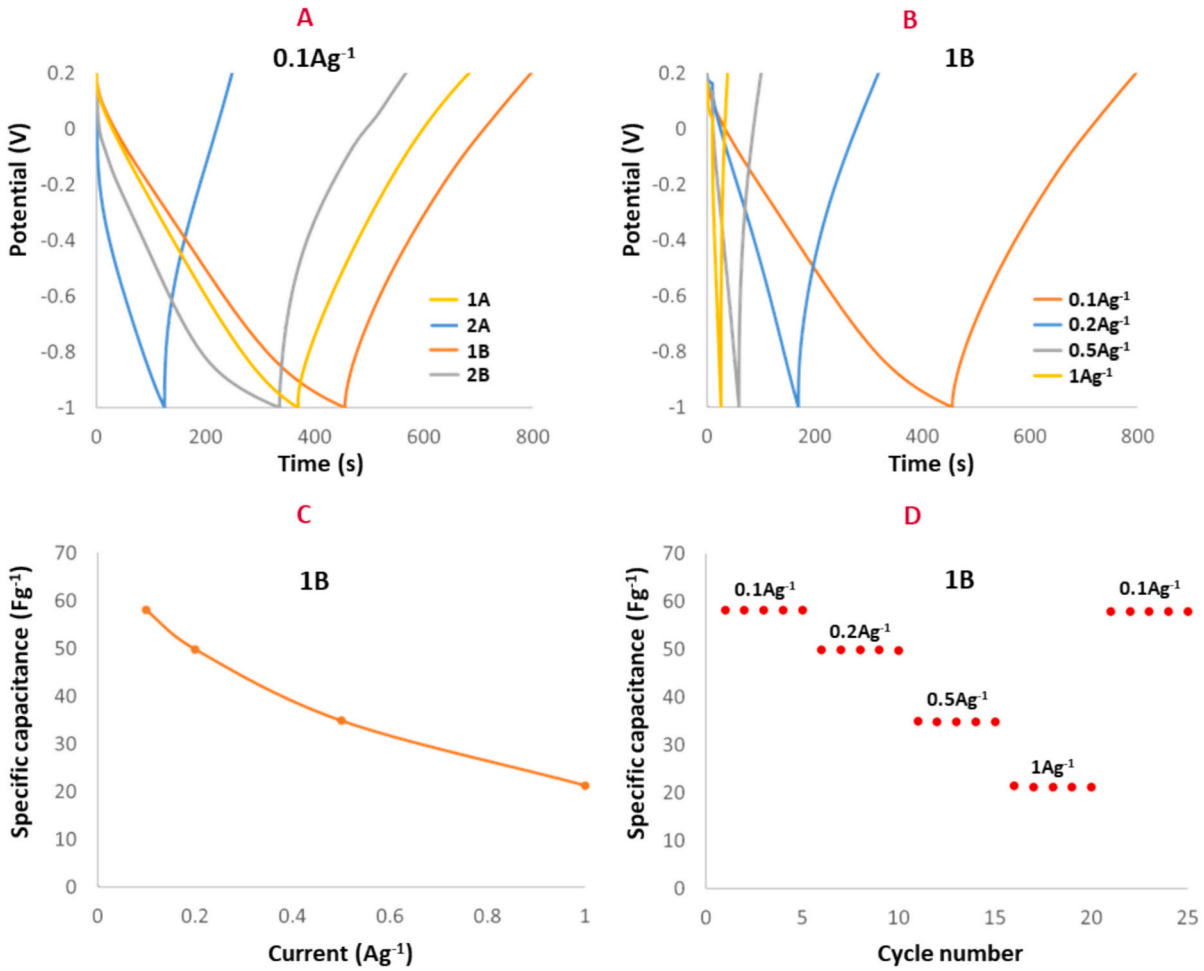


Fig. 10. A) Galvanostatic cycling of different CAs samples at 0.1 mAg^{-1}, B) Galvanostatic cycling of a 1B CA-based electrode at different current values, C) specific capacitance calculated from galvanostatic cycling of a 1B CA-based electrode at different currents, D) rate capability of a 1B CA-based electrode at different current values.

Table 7
Capacitance calculated according to Eq. (3) by galvanostatic cyclations data obtained at 0.1 Ag^{-1}.

Sample	Capacitance Fg^{-1}	Sample	Capacitance Fg^{-1}
1A	30.6	2A	10.4
1B	58.0	2B	27.9

abovementioned characteristics, this peak can be assigned to aromatic C═C bonds within the carbon aerogel matrix and carbon black component of the electrode [52–54]. The following contributions can be assigned to aliphatic defective sp^3 C atoms (285.0 eV, blue curves) [55], C—OH (hydroxyl, 286.45 eV, green curves), C═O (carbonyl, 288.40 eV, violet curves), and COOH (carboxyl, 289.15 eV, magenta curves) [54,56–58]. Furthermore, an additional couple of signals has been recorded, attributable to methylene and —CF_2— groups in PVDF binder

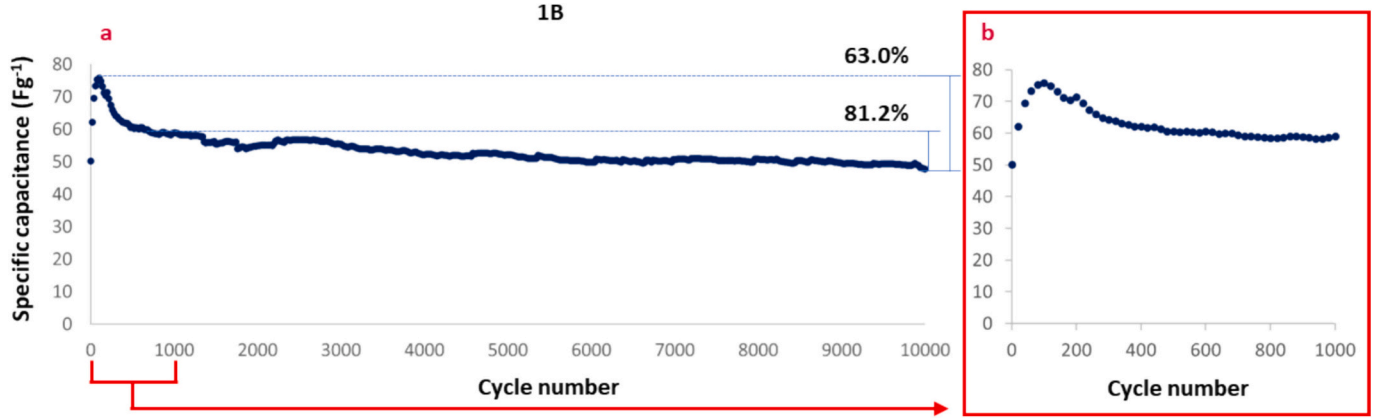


Fig. 11. Life cycle of a 1B CA-based electrode.

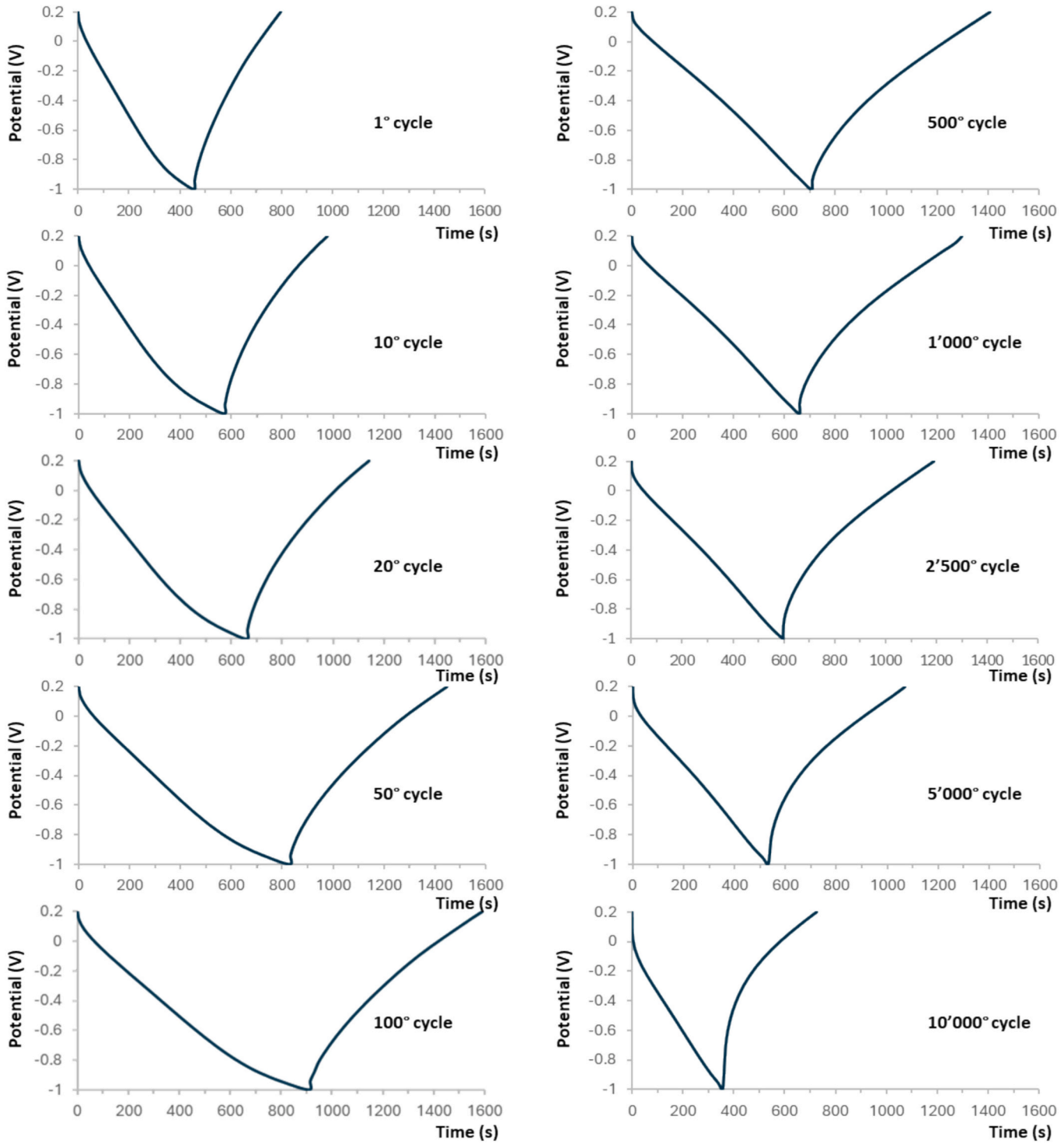


Fig. 12. Charge-discharge potential curves of 1B CA-based electrode at various cycles.

(287.55 and 292.25 eV, brown and orange curves, respectively) [59]. These two peaks appear positively shifted (~1.5 eV) with respect to the values reported in the literature, [59] probably due to a partial electrostatic charging of the PVDF fraction under X-ray irradiation for inefficacious charge compensation upon photoionization. This charging would also account for the residual intensity tail recorded at high BE (~294 eV, dashed grey line in Fig. 15 a). After cycling (Fig. 15 b), the same components can be found, but with slight intensity differences. Compared to the graphitic C═C atoms (red curves), a modest increase of defective sp^3 C (blue curves), C—OH (green curves) and COOH (magenta curves) functional groups can be appreciated, probably due to irreversible oxidation reactions occurring within the electrochemical cell upon cycling. Additionally, an intense K 2p contribution (grey curves) appears with a spin-orbit split doublet signal (K $2p_{3/2}$ at 292.9 eV, ΔE_{SO} = 2.8 eV) consistent with residuals from the KOH electrolyte used in the electrochemical cell.

4. Conclusions

A facile synthetic pathway was developed to obtain carbon aerogels

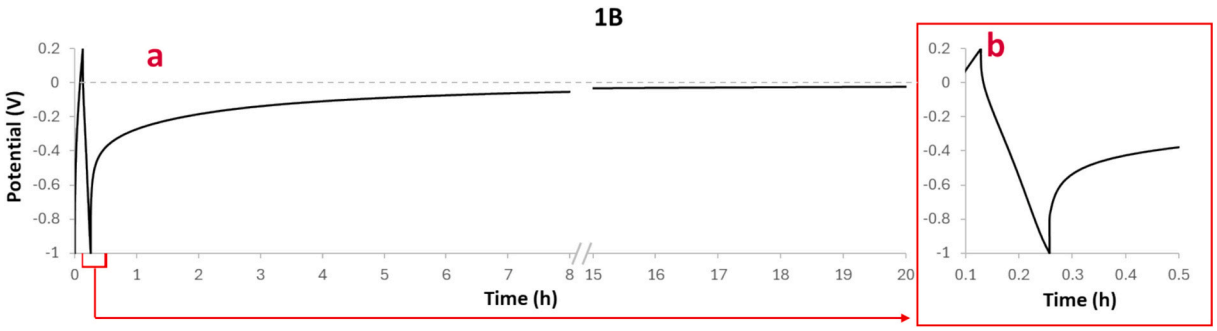


Fig. 13. Self-discharge of 1B CA-based electrode.

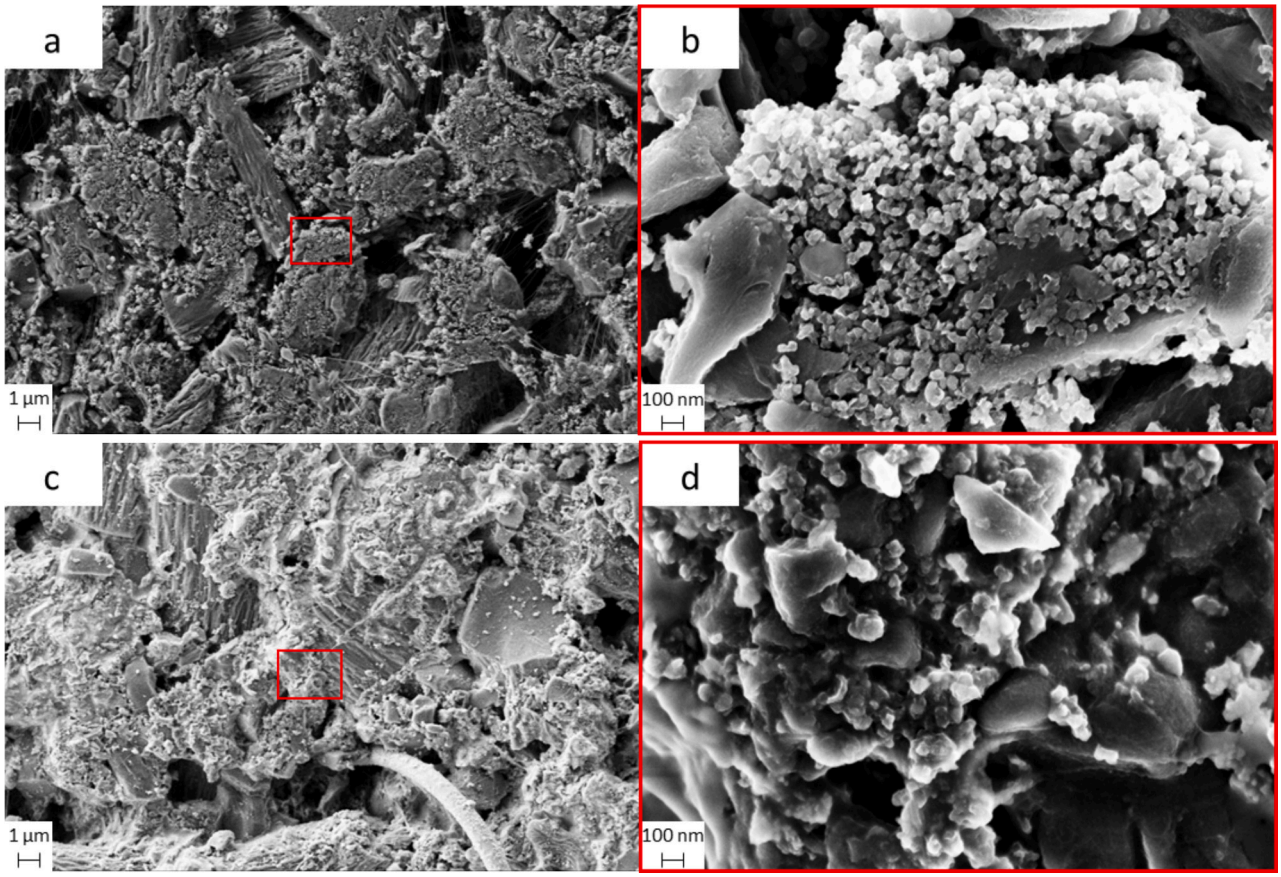


Fig. 14. SEM micrographs of a) pristine CAs electrode at 10× magnification, b) pristine CAs electrode at 100× magnification, c) CAs electrode after 1k cycles at 10× magnification, d) CAs electrode after 1k cycles at 100× magnification.

starting from rice husk. Some of the experimental conditions which mostly affect the properties of the aerogels were pointed out, and the whole process was optimized in terms of purity and yield. After a complete physico-chemical characterization, the obtained aerogels were used to prepare electrodes for supercapacitors. Despite not showing particularly exiting performances in terms of absolute values, one of the electrodes proved to be characterized by extraordinary long life, remarkable robustness and electrochemical stability, with a capacitance retention up to 63 % from the beginning and up to 81.2 % from cycle 500 to cycle 10,000. Without the well-known synergistic effect normally exploited for composite carbon-based electrodes, the obtained results are comparable to those of pyrolytic carbon synthesized from RH in harsher conditions, thus proving the robustness of our material and offering a promising perspective on green energy storage solutions.

CRediT authorship contribution statement

P. Atanasio: Writing – original draft, Visualization, Methodology, Investigation, Formal analysis, Conceptualization. **R.Y.S. Zampiva:** Writing – review & editing, Investigation. **A. Fornari:** Investigation. **C. Mancini:** Investigation. **A. Aurora:** Investigation. **A.G. Marrani:** Investigation. **M. Rossi:** Writing – review & editing, Supervision, Funding acquisition. **M. Pasquali:** Writing – review & editing, Supervision, Funding acquisition. **F.A. Scaramuzzo:** Writing – review & editing, Writing – original draft, Visualization, Funding acquisition, Formal analysis.

Declaration of competing interest

The authors declare that they have no known competing financial

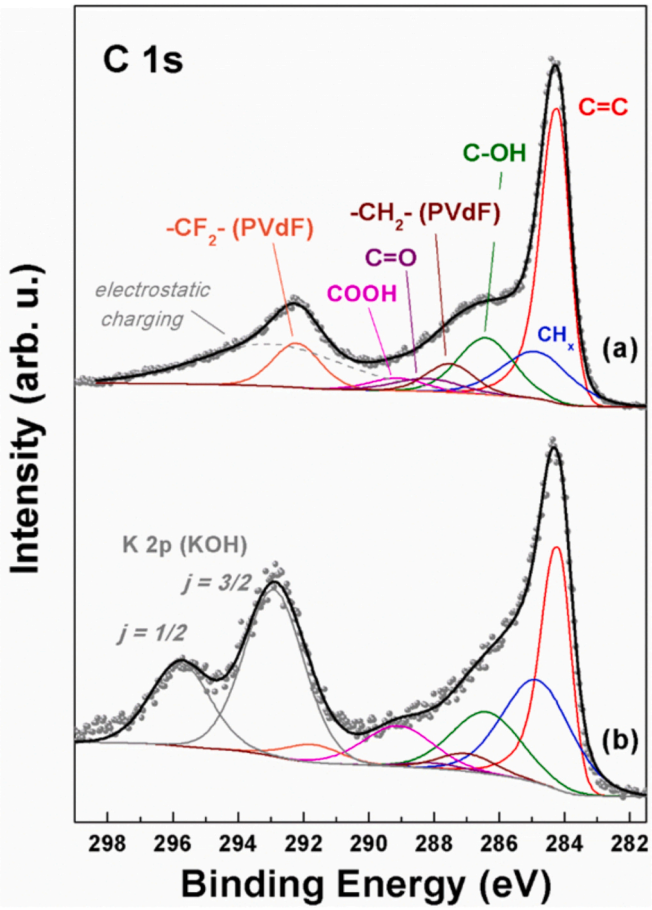


Fig. 15. XPS C 1s ionization region of (a) 1B CA-based pristine and (b) cycled electrode samples. Raw data are displayed with dots, while the curve-fitting reconstruction is represented by continuous coloured lines.

interests or personal relationships that could have appeared to influence the work reported in this paper.

Acknowledgements

Prof. Andrea Balducci, Institute for Technical Chemistry and Environmental Chemistry, University of Jena "F. Schiller", and Center for Energy and Environmental Chemistry (CEEC), Jena, Germany, is highly thanked for his invaluable help in BET analysis and fruitful discussions. Prof. Sergio Brutti, Department of Chemistry, Sapienza University of Rome, is kindly acknowledged for FTIR availability. The authors acknowledge the support of: (i) project Infrastructure for ENergy TRAnsition aNd Circular Economy @ EuroNanoLab (iENTRANCE@ENL) and its partners; (ii) ENEA (Agenzia nazionale per le nuove tecnologie, l'energia e lo sviluppo economico sostenibile) for the three-year 2022-2024 plan of research on national electric system (PIANO TRIENNALE DI REALIZZAZIONE 2022-2024 DELLA RICERCA DI SISTEMA ELETTRICO NAZIONALE). This study was carried out within the MOST – Sustainable Mobility Center and received funding from the European Union Next-GenerationEU (PIANO NAZIONALE DI RIPRESA E RESILIENZA (PNRR) – MISSIONE 4 COMPONENTE 2, INVESTIMENTO 1.4 – D.D. 1033 17/06/2022, CN00000023). This manuscript reflects only the authors' views and opinions, neither the European Union nor the European Commission can be considered responsible for them.

Appendix A. Supplementary data

Supplementary data to this article can be found online at https://doi.org/10.1016/j.est.2025.115901.

Data availability

Data will be made available on request.

References

[1] D. Londoño-Pulgarin, G. Cardona-Montoya, J.C. Restrepo, F. Muñoz-Leiva, Fossil or bioenergy? Global fuel market trends, Renewable and Sustainable Energy Reviews 143 (2021) 110905, https://doi.org/10.1016/j.rser.2021.110905.
[2] A. Dell'Era, M. Pasquali, G. Tarquini, F.A. Scaramuzzo, P. De Gasperis, P.P. Prosini, A. Mezzi, R. Tuffi, L. Cafiero, Carbon powder material obtained from an innovative high pressure water jet recycling process of tires used as anode in alkali ion (Li, Na) batteries, Solid State Ion. 324 (2018) 20–27, https://doi.org/10.1016/j.ssi.2018.06.008.
[3] A. Devi, S. Bajar, H. Kour, R. Kothari, D. Pant, A. Singh, Lignocellulosic biomass valorization for bioethanol production: a circular bioeconomy approach, Bioenergy Res. 15 (2022) 1820–1841, https://doi.org/10.1007/s12155-022-10401-9.
[4] P. Gomrokchi, M. Shabani-Nooshabadi, M. Ghiyasiyan-Arani, M. Salavati-Niasari, Tube-on-rod structure of MWCNTs-ammonium cobalt vanadium oxide/ammonium vanadium oxide; evaluation of electrochemical hydrogen storage capacity, J Energy Storage 85 (2024) 111041, https://doi.org/10.1016/j.est.2024.111041.
[5] F.A. Scaramuzzo, A. Pozio, A. Masci, F. Mura, A. Dell'Era, A. Curulli, M. Pasquali, Efficient photocurrent generation using a combined Ni-TiO_2 nanotubes anode, J. Appl. Electrochem. 45 (2015) 727–733, https://doi.org/10.1007/s10800-015-0837-9.
[6] A. Dell'Era, M. Pasquali, E.M. Bauer, S. Vecchio Ciprioti, F.A. Scaramuzzo, C. Lupi, Synthesis, characterization, and electrochemical behavior of $LiMn_xFe_{(1-x)}PO_4$ composites obtained from phenylphosphonate-based organic-inorganic hybrids, Materials 11 (2018) 56, https://doi.org/10.3390/ma11010056.
[7] A. Dell'Era, F.A. Scaramuzzo, M. Stoller, C. Lupi, M. Rossi, D. Passeri, M. Pasquali, Spinning disk reactor technique for the synthesis of nanometric sulfur TiO_2 core-shell powder for lithium batteries, Applied Sciences (Switzerland) 9 (2019) 1913, https://doi.org/10.3390/app9091913.
[8] X. Wu, X. Yang, B. Wang, J. Mu, X. Shen, P. Zhou, J. Zhou, S. Zhuo, Molten salt method derived porous carbon with high energy density in KI-additive electrolyte, J Energy Storage 74 (2023) 109253, https://doi.org/10.1016/j.est.2023.109253.
[9] G. Tarquini, A. Dell'Era, P.P. Prosini, F.A. Scaramuzzo, C. Lupi, M. Pasquali, Polysulfide solution effects on Li[sbnd]S batteries performances, J. Electroanal. Chem. 870 (2020) 114239, https://doi.org/10.1016/j.jelechem.2020.114239.
[10] H. Pourfarzad, M. Shabani-Nooshabadi, M.R. Ganjali, Novel bi-functional electrocatalysts based on the electrochemical synthesized bimetallicmetal organic frameworks: towards high energy advanced reversible zinc–air batteries, J. Power Sources 451 (2020) 227768, https://doi.org/10.1016/j.jpowsour.2020.227768.
[11] F.A. Scaramuzzo, M. Pasquali, F. Mura, A. Pozio, A. Dell'Era, A. Curulli, TiO_2 nanotubes photo-anode: an innovative cell design, Chem. Eng. Trans. 41 (2014) 223–228, https://doi.org/10.3303/CET1441038.
[12] F. Zahedi, M. Shabani-Nooshabadi, Porous structure Ni/$CuCo_2O_4$ core–shell as a novel type of three-dimensional electrode with facile fabrication and binder-free toward enhanced methanol oxidation and supercapacitor performances, Fuel 335 (2023) 127083, https://doi.org/10.1016/j.fuel.2022.127083.
[13] F. Cognigni, M. Pasquali, P.P. Prosini, C. Paoletti, A. Aurora, F.A. Scaramuzzo, M. Rossi, X-ray microscopy: a non-destructive multi-scale imaging to study the inner workings of batteries, ChemElectroChem 10 (2023) e202201081, https://doi.org/10.1002/celc.202201081.
[14] D. Dini, F. Cognigni, D. Passeri, F.A. Scaramuzzo, M. Pasquali, M. Rossi, Review—multiscale characterization of Li-ion batteries through the combined use of atomic force microscopy and X-ray microscopy and considerations for a correlative analysis of the reviewed data, J. Electrochem. Soc. 168 (2021) 126522, https://doi.org/10.1149/1945-7111/ac4298.
[15] H. Pourfarzad, M. Shabani-Nooshabadi, M.R. Ganjali, M.H. Olia, Inhibition of acid corrosion of glass ampoule in Pb/HBF_4/PbO_2 reserve batteries using nanobis[3-(trimethoxysilyl)propyl]amine, J. Mol. Liq. 302 (2020) 112578, https://doi.org/10.1016/j.molliq.2020.112578.
[16] H. Pourfarzad, M. Shabani-Nooshabadi, M.R. Ganjali, High lithium anodic performance of reduced Sn particles on Co metal-organic frameworks for lithium-ion batteries with a long-cycle life, Compos B Eng 193 (2020) 108008, https://doi.org/10.1016/j.compositesb.2020.108008.
[17] S.V. Vassilev, D. Baxter, L.K. Andersen, C.G. Vassileva, An overview of the chemical composition of biomass, Fuel 89 (2010) 913–933, https://doi.org/10.1016/j.fuel.2009.10.022.
[18] M. Kordi, N. Farrokhi, M.I. Pech-Canul, A. Ahmadikhah, Rice husk at a glance: from agro-industrial to modern applications, Rice Sci. 31 (2024) 14–32, https://doi.org/10.1016/j.rsci.2023.08.005.
[19] P. Atanasio, R.Y.S. Zampiva, L. Buccini, C. Di Conzo, A. Proietti, F. Mura, A. Aurora, A.G. Marrani, D. Passeri, M. Rossi, M. Pasquali, F.A. Scaramuzzo, Graphene quantum dots from agricultural wastes: green synthesis and advanced applications for energy storage, Molecules 29 (2024) 5666, https://doi.org/10.3390/molecules29235666.

[20] H. Pourfarzad, M. Shabani-Nooshabadi, M.R. Ganjali, H. Kashani, Synthesis of Ni–Co-Fe layered double hydroxide and Fe_2O_3/graphene nanocomposites as actively materials for high electrochemical performance supercapacitors, Electrochim. Acta 317 (2019) 83–92, https://doi.org/10.1016/j.electacta.2019.05.122.
[21] H. Ansarinejad, M. Shabani-Nooshabadi, S.M. Ghoreishi, Enhanced supercapacitor performance using a Co_3O_4@Co_3S_4 nanocomposite on reduced graphene oxide/Ni foam electrodes, Chem. Asian J. 16 (2021) 1258–1270, https://doi.org/10.1002/asia.202100124.
[22] H. Ansarinejad, M. Shabani-Nooshabadi, S.M. Ghoreishi, Facile synthesis of crumpled-paper like $CoWO_4$-$CoMn_2O_4$/N-doped graphene hybrid nanocomposites for high performance all-solid-state asymmetric supercapacitors, J Energy Storage 45 (2022) 103513, https://doi.org/10.1016/j.est.2021.103513.
[23] A. Meftahi, M. Shabani-Nooshabadi, A. Reisi-Vanani, Introducing GO/CuI nanostructure as active electrode matter for supercapacitors: a comparative investigation within two aqueous electrolytes, J Energy Storage 63 (2023) 107077, https://doi.org/10.1016/j.est.2023.107077.
[24] M. Sajjad, M.I. Khan, F. Cheng, W. Lu, A review on selection criteria of aqueous electrolytes performance evaluation for advanced asymmetric supercapacitors, J Energy Storage 40 (2021) 102729, https://doi.org/10.1016/j.est.2021.102729.
[25] H.C. Chien, W.Y. Cheng, Y.H. Wang, S.Y. Lu, Ultrahigh specific capacitances for supercapacitors achieved by nickel cobaltite/carbon aerogel composites, Adv. Funct. Mater. 22 (2012) 5038–5043, https://doi.org/10.1002/adfm.201201176.
[26] J.H. Lee, S.J. Park, Recent advances in preparations and applications of carbon aerogels: a review, Carbon N Y 163 (2020) 1–18, https://doi.org/10.1016/j.carbon.2020.02.073.
[27] M. Karimi Anjiraki, M. Ghiyasiyan-Arani, Z. Falah Khudair, M. Baladi, M. Shabani-Nooshabadi, M. Salavati-Niasari, A highly efficient $PrMnO_3$/graphene oxide nanocomposite for visible light induced photocatalytic water treatment, Sol. Energy 275 (2024) 112615, https://doi.org/10.1016/j.solener.2024.112615.
[28] M. Karimi Anjiraki, M. Ghiyasiyan-Arani, M. Baladi, F.H. Alsultany, M. Shabani-Nooshabadi, M. Salavati-Niasari, Magnetically recyclable $PrFeO_3$/g-C_3N_4 nano-photocatalyst with Z-scheme structure: synthesis and characterization and its application for enhanced degradation of malachite green as contaminated water under sunlight, Inorg. Chem. Commun. 170 (2024) 113184, https://doi.org/10.1016/j.inoche.2024.113184.
[29] P. Jõul, T.T. Ho, U. Kallavus, A. Konist, K. Leiman, O.S. Salm, M. Kulp, M. Koel, T. Lukk, Characterization of organosolv lignins and their application in the preparation of aerogels, Materials 15 (2022) 2861, https://doi.org/10.3390/ma15082861.
[30] E. Melro, L. Alves, F.E. Antunes, B. Medronho, A brief overview on lignin dissolution, J. Mol. Liq. 265 (2018) 578–584, https://doi.org/10.1016/j.molliq.2018.06.021.
[31] L. Tang, Y. Feng, W. He, F. Yang, Combination of graphene oxide with flax-derived cellulose dissolved in NaOH/urea medium to generate hierarchically structured composite carbon aerogels, Ind. Crop. Prod. 130 (2019) 179–183, https://doi.org/10.1016/j.indcrop.2018.12.068.
[32] L. Wang, Q. Wu, B. Zhao, Z. Li, Y. Zhang, L. Huang, S. Yu, Multi-functionalized carbon aerogels derived from chitosan, J. Colloid Interface Sci. 605 (2022) 790–802, https://doi.org/10.1016/j.jcis.2021.07.132.
[33] F.E.C. Othman, N.A.H.M. Nordin, N. Ismail, H.S. Zakria, H. Junoh, M.H.A. Aziz, A review on sustainable graphene production from rice husks: strategies and key considerations, Chem. Eng. J. 497 (2024) 154408, https://doi.org/10.1016/j.cej.2024.154408.
[34] A. Meftahi, M. Shabani-Nooshabadi, A. Reisi-Vanani, AgI/g-C3N4 nanocomposite as electrode material for supercapacitors: comparative study for its efficiency in three different aqueous electrolytes, Electrochim. Acta 430 (2022) 141052, https://doi.org/10.1016/j.electacta.2022.141052.
[35] A. Meftahi, A. Reisi-Vanani, M. Shabani-Nooshabadi, Comparison of performance of CuI/g-C3N4 nanocomposites synthesized on Ni-foam and graphitic substrates as suitable electrode materials for supercapacitors, Fuel 331 (2022) 125683, https://doi.org/10.1016/j.fuel.2022.125683.
[36] M. Ghiyasiyan-Arani, H. Ansarinejad, M. Shabani-Nooshabadi, E.A. Dawi, M. Salavati-Niasari, Design 3D hierarchical flower-shaped $NH_4V_4O_{10}$/N-GQDs/cellulose nanocomposites as electrode materials for supercapacitor application, J. Alloys Compd. 976 (2024) 173205, https://doi.org/10.1016/j.jallcom.2023.173205.
[37] N.A.M. Barakat, M.S. Mahmoud, H.M. Moustafa, Comparing specific capacitance in rice husk-derived activated carbon through phosphoric acid and potassium hydroxide activation order variations, Sci. Rep. 14 (2024) 1460, https://doi.org/10.1038/s41598-023-49675-0.
[38] L. Wang, Q. Wu, B. Zhao, Z. Li, Y. Zhang, L. Huang, S. Yu, Multi-functionalized carbon aerogels derived from chitosan, J. Colloid Interface Sci. 605 (2022) 790–802, https://doi.org/10.1016/j.jcis.2021.07.132.
[39] S. Hoepfner, L. Ratke, B. Milow, Synthesis and characterisation of nanofibrillar cellulose aerogels, Cellulose 15 (2008) 121–129, https://doi.org/10.1007/s10570-007-9146-8.
[40] G. Cheng, P. Varanasi, R. Arora, V. Stavila, B.A. Simmons, M.S. Kent, S. Singh, Impact of ionic liquid pretreatment conditions on cellulose crystalline structure using 1-ethyl-3-methylimidazolium acetate, J. Phys. Chem. B 116 (2012) 10049–10054, https://doi.org/10.1021/jp304538v.
[41] C.R. Bauli, D.B. Rocha, S.A. de Oliveira, D.S. Rosa, Cellulose nanostructures from wood waste with low input consumption, J. Clean. Prod. 211 (2019) 408–416, https://doi.org/10.1016/j.jclepro.2018.11.099.
[42] R. Bardestani, G.S. Patience, S. Kaliaguine, Experimental methods in chemical engineering: specific surface area and pore size distribution measurements—BET, BJH, and DFT, Can. J. Chem. Eng. 97 (2019) 2781–2791, https://doi.org/10.1002/cjce.23632.
[43] S.M. Jung, D. Lopes Mafra, C.T. Lin, H.Y. Jung, J. Kong, Controlled porous structures of graphene aerogels and their effect on supercapacitor performance, Nanoscale 7 (2015) 4386, https://doi.org/10.1039/c4nr07564a.
[44] G. Zu, J. Shen, L. Zou, F. Wang, X. Wang, Y. Zhang, X. Yao, Nanocellulose-derived highly porous carbon aerogels for supercapacitors, Carbon N Y 99 (2016) 203–211, https://doi.org/10.1016/j.carbon.2015.11.079.
[45] G.H. Jin, S. Wu, T. Li, Y. Bai, X. Wang, H. Zhang, H. Xu, C. Kong, H. Wang, Synthesis of porous carbon nano-onions derived from rice husk for high-performance supercapacitors, Appl. Surf. Sci. 488 (2019) 593–599, https://doi.org/10.1016/j.apsusc.2019.05.308.
[46] K. Liu, C. Yu, W. Guo, L. Ni, J. Yu, Y. Xie, Z. Wang, Y. Ren, J. Qiu, Recent research advances of self-discharge in supercapacitors: mechanisms and suppressing strategies, Journal of Energy Chemistry 58 (2021) 94–109, https://doi.org/10.1016/j.jechem.2020.09.041.
[47] Q.D. Nguyen, Y.H. Wu, T.Y. Wu, M.J. Deng, C.H. Yang, J.K. Chang, Gravimetric/volumetric capacitances, leakage current, and gas evolution of activated carbon supercapacitors, Electrochim. Acta 222 (2016) 1153–1159, https://doi.org/10.1016/j.electacta.2016.11.087.
[48] T. Cai, H. Wang, C. Jin, Q. Sun, Y. Nie, Fabrication of nitrogen-doped porous electrically conductive carbon aerogel from waste cabbage for supercapacitors and oil/water separation, J. Mater. Sci. Mater. Electron. 29 (2018) 4334–4344, https://doi.org/10.1007/s10854-017-8381-5.
[49] L. Zeng, X. Lou, J. Zhang, C. Wu, J. Liu, C. Jia, Carbonaceous mudstone and lignin-derived activated carbon and its application for supercapacitor electrode, Surf. Coat. Technol. 357 (2019) 580–586, https://doi.org/10.1016/j.surfcoat.2018.10.041.
[50] X. Sun, H. Shiraz, R. Wong, J. Zhang, J. Liu, J. Lu, N. Meng, Enhancing the performance of PVDF/GO ultrafiltration membrane via improving the dispersion of GO with homogeniser, Membranes 12 (2022) 1268, https://doi.org/10.3390/membranes12121268.
[51] https://www.chemicalbook.com/SpectrumEN_1310-58-3_IR1.htm.
[52] A.G. Marrani, A.C. Coico, D. Giacco, R. Zanoni, F.A. Scaramuzzo, R. Schrebler, D. Dini, M. Bonomo, E.A. Dalchiele, Integration of graphene onto silicon through electrochemical reduction of graphene oxide layers in non-aqueous medium, Appl. Surf. Sci. 445 (2018) 404–414, https://doi.org/10.1016/j.apsusc.2018.03.147.
[53] A. Kovtun, D. Jones, S. Dell'Elce, E. Treossi, A. Liscio, V. Palermo, Accurate chemical analysis of oxygenated graphene-based materials using X-ray photoelectron spectroscopy, Carbon 143 (2019) 268–275, https://doi.org/10.1016/j.carbon.2018.11.012.
[54] R. Larciprete, P. Lacovig, S. Gardonio, A. Baraldi, S. Lizzit, Atomic oxygen on graphite: chemical characterization and thermal reduction, J. Phys. Chem. C 116 (2012) 9900–9908, https://doi.org/10.1021/jp2098153.
[55] H. Estrade-Szwarckopf, XPS photoemission in carbonaceous materials: a "defect" peak beside the graphitic asymmetric peak, Carbon 42 (2004) 1713–1721, https://doi.org/10.1016/j.carbon.2004.03.005.
[56] D. Briggs, M.P. Seah, Practical Surface Analysis, 2nd ed., Chichester, UK, J. Wiley & Sons, 1990.
[57] F. Tiberio, F. Vincenzoni, F. Amato, C. Desiderio, G. Perini, I. Moretti, A. Augello, G. Friggeri, L. Cui, L. Giaccari, M. Salvati, L. Polito, O. Parolini, M. De Spirito, A. G. Marrani, W. Lattanzi, M. Papi, V. Palmieri, The osteoconductive properties of graphene-based material surfaces are finely tuned by the conditioning layer and surface chemistry, Mater. Adv. 5 (2024) 4772, https://doi.org/10.1039/D4MA00144C.
[58] I. Ferrari, A. Motta, F. Amato, E.A. Dalchiele, A.G. Marrani, Assessing the evolution of oxygenated functional groups on the graphene oxide surface upon mild thermal annealing in water, RSC Adv. 13 (2023) 29308, https://doi.org/10.1039/D3RA05083A.
[59] G. Beamson, D. Briggs, High Resolution XPS of Organic Polymers: The Scienta ESCA300 Database, J. Wiley & Sons, Chichester, UK, 1992.